Ocean surface currents directly imaged from space

Nicolas Rascle[1,2*], Aurélien Ponte[1], Frédéric Nouguier[1], Renaud Binet[3], Dhruv Balwada[4], Fabrice Ardhuin[1], Bertrand Chapron[1], Erwin Bergsma[3], Fabrice Collard[5], Louis Marié[1], Rafael Almar[6]

[1*]LOPS, Ifremer-Univ. Brest-CNRS-IRD, Plouzané, 29200, France.
[2*]DOF, CICESE, Ensenada, 22860, Mexico.
[3]EOL, CNES, Toulouse, 31400, France.
[4]LDEO, Columbia Univ., New York, 10964, USA.
[5]OceanDataLab, Plouzané, 29280, France.
[6]LEGOS, CNRS-IRD-CNES-Univ. Toulouse, Toulouse, 31400, France.

*Corresponding author(s). E-mail(s): nicolas.rascle@ifremer.fr;

Abstract

For more than four decades, satellite images of ocean temperature and colour have revealed jets, swirling eddies, and filaments[1–3]. Yet the currents that shape these structures have never been directly imaged from space. This observational gap limits our understanding of the ocean's impact on climate[4] and marine ecosystems[5], as these currents modulate exchanges between the coast and open ocean, vertical transport to the deep sea, and fluxes of heat, carbon, and nutrients[6–11].

Here we demonstrate the first direct satellite imaging of kilometre-scale surface currents using a tandem configuration of optical satellites that tracks surface wave propagation. This new capability shifts satellite observations beyond the predominantly geostrophic view of ocean circulation, revealing dynamics that have remained largely invisible to satellites – from intense coastal jets and equatorial flows to submesoscale motions just kilometres wide. Across these regimes, the elusive divergence of fronts and internal waves, thought to play a key role in upper-ocean vertical exchange, is concentrated at scales below 5 km, previously unresolved from space. These reference measurements provide a new observational window into the multiscale physics of the upper ocean and its mediating role for the Earth's climate system and marine life.

Preprint non peer-reviewed, submitted in September 2026: manuscript currently under review at *Nature Communications*

Ocean currents shape climate, ecosystems, and ultimately human activities. They transport heat, nutrients and carbon, structure marine biodiversity, and disperse pollutants. Yet our understanding of these motions remains incomplete, just as the need for it grows—from a warming climate and declining biodiversity to the nascent push toward blue economy and marine carbon dioxide removal[4].

The large scale circulation of the upper-ocean has been known since the latter half of the twentieth century, and satellite observations since the 1980s have mapped the mesoscale (100 km) circulation. Away from the equator, these motions approximately follow the geostrophic balance, in which the pressure gradient opposes the Coriolis force, causing sea-surface height (SSH) to mirror the underlying currents. Thanks to SSH observations from satellite altimetry, this regime – and the way eddies reshape horizontal ocean transport – is now relatively well understood[12,13].

Yet in the past two decades, it has become evident that major blind spots remain, with two broad classes of currents escaping detection by traditional altimeters. The first comprises flows at scales of 1-50 km – the so-called submesoscales – too small to be resolved. The second further extends to other ageostrophic currents, such as equatorial jets (where the Coriolis force vanishes), wind-driven flows (dominated by wind stress) and tidal or wave-like currents (governed by acceleration).

Numerical models suggest that these undetected currents are pivotal. They likely regulate exchanges between the coast and open ocean[6], structure marine ecosystems[5,7], and influence the dispersal of floating matter, from oil slicks to Sargassum mats[8]. Crucially, the vertical velocities that connect the surface and deep ocean occur primarily at submesoscales, suggesting a key role in the ocean interior ventilation and in the fluxes of heat, carbon, nutrients, and energy that shape Earth's climate[9–11,14,15].

Despite their recognized importance, observing ageostrophic and submesoscale ocean currents remains a challenge. Dedicated field campaigns have provided invaluable insight into the processes at play[8,16,17], but how these findings generalize across the diversity of ocean basins and seasons remains an open question. Satellite imagery, in principle, could help overcome this limitation. Kilometer-scale images of sea surface temperature, colour and roughness have long fascinated oceanographers, revealing jets, swirling eddies and filaments[1–3] (see e.g. Fig. 2d, Extended fig 1d, Fig. 5f). Yet these images only hint at the underlying dynamics: the currents themselves have never been directly imaged.

A significant advance was recently achieved with the extension of traditional along-track altimetry into a swath system – the SWOT satellite[18] – which now precisely captures geostrophic flows down to 20 to 30 km[19–21]. Its striking sub-kilometre SSH images hint at access to even smaller scales[22], raising the prospect of resolving key ageostrophic processes such as horizontal divergence and the associated vertical velocities essential for climate. Yet instrument noise and internal-wave imprints on SSH demand advanced reconstruction methods and, consequently, independent observations for calibration and validation[23–26]. More direct current measurements using Doppler radar offer a complementary approach. They have been demonstrated from aircraft and proposed for future satellite missions[27,28], but present-day implementations remain limited to single-component measurements and are constrained by wave-induced velocity biases[29–32]. Other recently proposed techniques reconstruct current fields from temperature temporal evolution observed by geostationary satellites[33]. These neural network approaches provide extensive spatio-temporal coverage but are trained exclusively on numerical simulations and therefore require independent observations to validate the reconstructed submesoscale fields.

Given these limited observations to date, our understanding of submesoscale and ageostrophic currents still relies primarily on numerical models. Yet these models diverge at fine scales[34], partly due to differences in turbulence parameterizations and numerical schemes. These discrepancies are expected to increase as next-generation models incorporate additional dynamical feedbacks – internal waves, ocean-atmosphere coupling, surface-wave effects, and nonhydrostatic processes – potentially revealing new dynamical regimes. Identifying where new physics matters will require observations at the same fine scales models aim to resolve.

Here we demonstrate that a simple tandem configuration of optical satellites enables direct imaging of kilometre-scale surface currents, providing new observations of submesoscale and ageostrophic flows that help fill this long-standing observational gap.

Observations using an optical tandem of satellites

The new optical tandem (OT) approach (Fig.1 and Method 1) exploits a well-established principle: from successive optical images, we track the displacement of short surface waves, very abundant compared to rare surface slicks[35,36]. Because the wavelengths are resolved from space, the wave intrinsic phase speeds can be separated from the apparent motions, revealing the underlying current — a technique known as the wave-phase method.

This approach is among the most direct ways to observe surface currents, producing measurements that are non-invasive[37], calibration-free, and easily interpretable because they rely firmly on linear wave theory. The method is widely used, from HF radars to video imagery of X-band radars and airborne optical systems[38–40]. Applying it to satellite imagery, however, has proved difficult because only a few snapshots are typically available. Previous attempts using the Sentinel-2 satellite, with image pairs separated by only one second, detected only the strongest flows, limiting their value for studying ocean dynamics[41–43].

The new OT observing strategy relies on a simple tandem configuration of the Sentinel-2 constellation during calibration phases (see Materials) and introduces three key advances. (i) The time lag is increased by more than one order of magnitude, from 1 to 30 s. (ii) Despite the long time lag, coherence remains remarkably high owing to the identical viewing geometry of the two satellites, whereas it would rapidly decay in single-satellite imagery. (iii) Individual wave crests cannot be tracked anymore because each undergoes an unknown number of phase cycles during that time. Instead, we globally track multiple wave components within the wind-sea (Fig. 1 and Method 1). The underlying current is revealed with a dramatic noise decrease, thanks to the extended temporal lag. This enables to map the current at 1 km resolution, with each grid cell retrieved independently.

The current fields are validated against independent current measurements from swath altimetry, HF radars and drifters (Method 2), suggesting an accuracy better

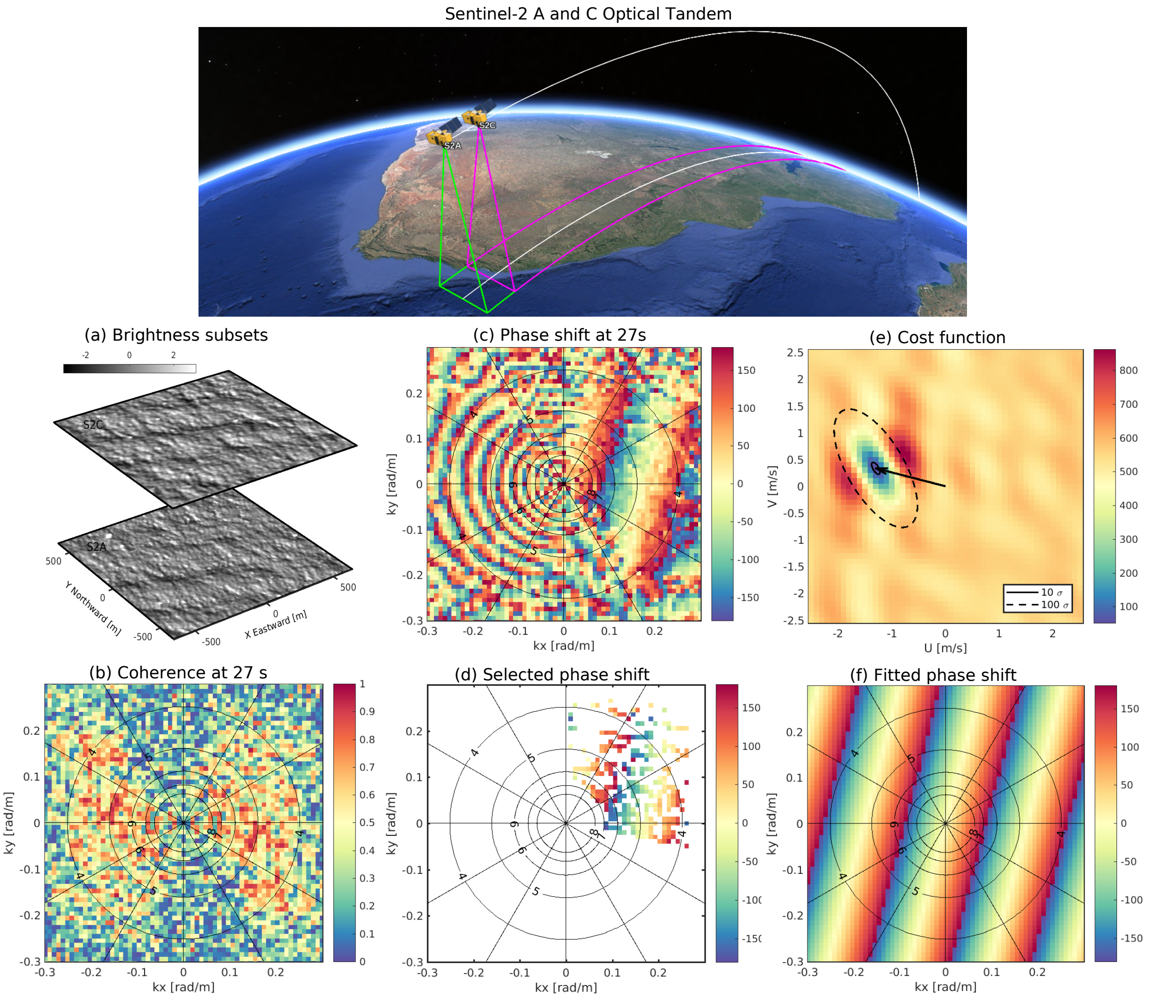

Fig. 1 Current retrieval from Sentinel-2 Optical Tandem imagery. Flying along the same orbit and separated by 27 s, the two satellites provide images from identical viewing angles. The example image subsets (nominal size 1.3 km) are located within a meander of the Agulhas Current, where the flow reaches about 1.3 m/s toward the northwest. From the two brightness images **(a)**, the coherence **(b)** and phase shift **(c)** are computed. Wave propagation ambiguity, low energy and low coherence components are discarded **(d)** before a global search over all possible current vectors **(e)** identifies the best-fitting phase shift **(f)** in a least-squares sense. The current uncertainty (1σ) shown in (e) is 0.5 cm s^{-1} in the dominant wave direction and 1.2 cm s^{-1} in the perpendicular direction.

than 20 cm s^{-1} for each component, likely approaching the limit of the intercomparison. Analysis of coherence and wave phase noise indicates a measurement precision of around 1 cm s^{-1}. Although no coincident current observations at kilometre resolution are available for direct verification, the sharp correspondence between current gradients and temperature, color and roughness fronts (Method 2), together with the structure function analysis (Method 4), consistently suggests a precision better than 4 cm s^{-1}.

Sentinel-2 OT, although limited to cloud-free and favourable wave conditions (see Material), expands our ability to observe ocean currents from space.

A new window on ocean currents

This new measurement approach shifts satellite observations beyond the predominantly geostrophic regime, revealing scales and dynamics previously inaccessible from space. Two key properties enable this capability. First, the measurements retrieve currents more directly than altimetry, which infers motion from sea-surface height. This allows detection of flows with weak or complex sea-level signatures – such as equatorial, tidal and wind-driven currents, as well as persistent coastal jets. Second, they achieve a one-kilometre resolution, whereas existing satellite techniques seldom resolve scales under 20 km, and only for a single velocity component in the case of radars with synthetic aperture[19,32]. Achieving such resolution with radars is not only technically demanding but also physically constrained, as radar Doppler velocities integrate contributions across wavenumbers, thereby intrinsically entangling coupled wind-wave-current signals[31].

This new observational window onto previously inaccessible scales and dynamical regimes is illustrated next through three representative examples: (i) submesoscale processes including ageostrophic fronts, filaments and divergent motions that shape tracer transport, ecosystems and climate-relevant fluxes; (ii) equatorial flows and internal waves, which are fundamental to climate variability and energy pathways; and (iii) large-scale coastal-trapped currents, which connect the coastal and open ocean.

Oceanic submesoscale regime

As a first case, we examine the Agulhas Current, a well-documented western boundary current, where OT reveals submesoscale dynamics from the shelf to the open-ocean (Fig. 2a-c). The low measurement noise allows direct estimation of flow spatial deformations, quantified by vorticity, divergence and strain (Method 4). An independent sea surface temperature (SST) observation was acquired by the Sentinel-3 satellite 29 minutes before OT (Fig. 2d).

The Agulhas Current appears bounded by sharp, elongated gradients only a few kilometres wide. Thermal and velocity fronts exhibit tight spatial collocation, mostly within 3 km (see Method 2 and the superimposable full-resolution panels provided in Data S1). This match between independent satellites and observed variables provides a convincing hint that OT accurately retrieves fine-scale currents. Vorticity outlines a web of interspersed filaments, with few isolated eddies, and reveals a marked dominance of cyclonic vorticity. Divergence, a marker of possible vertical exchanges between the surface and subsurface ocean, is primarily organized in patchy regions around fronts and filaments, with alternating signs across these structures and only a few possible internal-wave signatures (see next section).

Many of these features are consistent with previous regional in situ measurements[44–46], and fall within the range of behaviour exhibited by submesoscale numerical

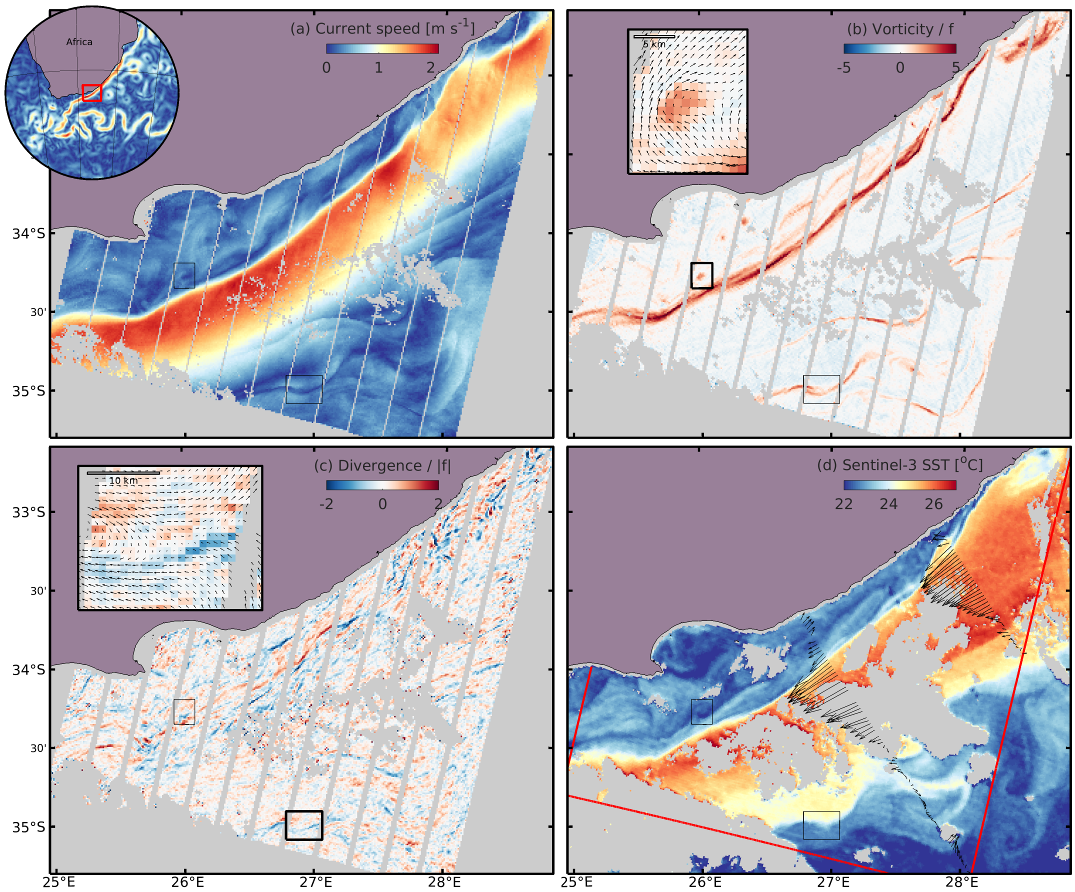

Fig. 2 Submesoscale and ageostrophic currents in the Agulhas region. (a-c) Currents derived from Sentinel-2 Optical Tandem on 11 Dec 2024 at 08:20 UTC. **(a)** Current magnitude (vectors omitted for readability). The globe inset shows the broader Agulhas system observed from nadir altimeters (AVISO). **(b,c)** Relative vorticity and divergence, normalized by planetary vorticity f. Insets highlight the fine scale structures associated with a shelf eddy and a spiraling front, with current vectors shown at full 1 km resolution. **(d)** Sea surface temperature observed 29 minutes earlier (07:51 UTC) by Sentinel-3 at 1 km resolution. Note the close alignment of independently observed current and temperature fronts. Two OT transects across the Agulhas are superimposed on the temperature. Transects are downsampled at 2.5 km for readability. Grey areas denote missing data due to clouds or water depth less than 30 m.

models[34,47] and targeted process studies[8,16,17]. The key advance is the ability to observe these features from space, enabling their mapping over large areas (Fig. 2) and their dynamical quantification (Fig. 3) – often for the first time. For instance, shelf cyclones are detected (inset of Fig. 2b), each only 5 km-wide and reaching vorticities of about 5 f (with f the local Coriolis parameter), confirming the ability to map strongly ageostrophic structures previously accessible only to localized in-situ observations[46]. Except in isolated regions, the internal Agulhas front seldom exceeds 5 f in vorticity and rarely sharpens below 2-3 km, which likely corresponds to the scale of frontal arrest[48]. In the study region, vorticity exceeds $f/2$ over about 30% of the area, indicating that ageostrophic dynamics are widespread, with advection comparable to the Coriolis force. We also recover expected signatures of submesoscale frontal dynamics in the joint distribution of vorticity and strain (Fig. 3c), in particular the cyclonic vorticity-strain tail associated with convergence, characteristic of mid-latitude fronts[16,49]. These statistics, together with current divergence itself, are directly observed from space for the first time[33].

Beyond these expected signatures, several features emerge that challenge current models and observations. One is the smooth and coherent texture of the Agulhas Current core: the velocity magnitude remains nearly uniform along a 300 km stretch of the flow (transect in Extended fig 2 inset c), with little sign of instability, internal waves or bathymetry-induced lee waves[50]. Such smoothness is surprising for the velocity field of a highly energetic current and differs from some numerical simulations where the Agulhas is prone to lee waves (see Movie S1 around 34.5°S 26°E and Method 5). This smooth jet also contrasts with recent swath altimetry, which portrays an ocean with more instabilities (Extended fig 2c,d). Another unexpected feature is the weak current variability at scales in the 1-10 km range, as evidenced by second-order structure functions (Fig. 3a and Method 4) exhibiting power laws slopes between $r^{2/3}$ to $r^{3/2}$ (corresponding to $k^{-5/3}$ to $k^{-5/2}$ power spectra), whereas the most recent airborne radar measurements and coupled wave-current models suggest substantially shallower spectra[51] (Extended fig 3a). This weak small-scale variability is remarkable given that OT velocities are unfiltered.

These contrasting observations of the submesoscale regime require reconciliation, as they have important implications for the ocean transport and energy cascade and may indicate inconsistencies in either modelled fine-scale dynamics or other observing frameworks. More broadly, this new observational window enables direct links between submesoscales and ecosystem structures, as illustrated in the less energetic coastal waters of New Zealand (Extended fig 1), where OT reveals the currents structuring a phytoplankton bloom.

A notable result is that divergence is concentrated at scales finer than 5 km, which contain 90% of its variance (red triangles in Fig. 3b and Extended fig 3b; Method 4). This concentration of divergence at kilometric scales may partly reflect the now-resolved internal waves (next section), but the most intense divergence events are significantly clustered around SST fronts (Method 4), indicating that frontal dynamics are an important contributor. These observations support longstanding hypotheses that kilometre-scale processes play a central role in upper-ocean vertical exchange and imply stringent spatial-resolution requirements for both satellite observations and numerical models.

Equatorial and internal wave regimes

Our second case focuses on the ocean circulation near the equator -an important region for the climate- which has remained inaccessible to altimetry because the Coriolis force

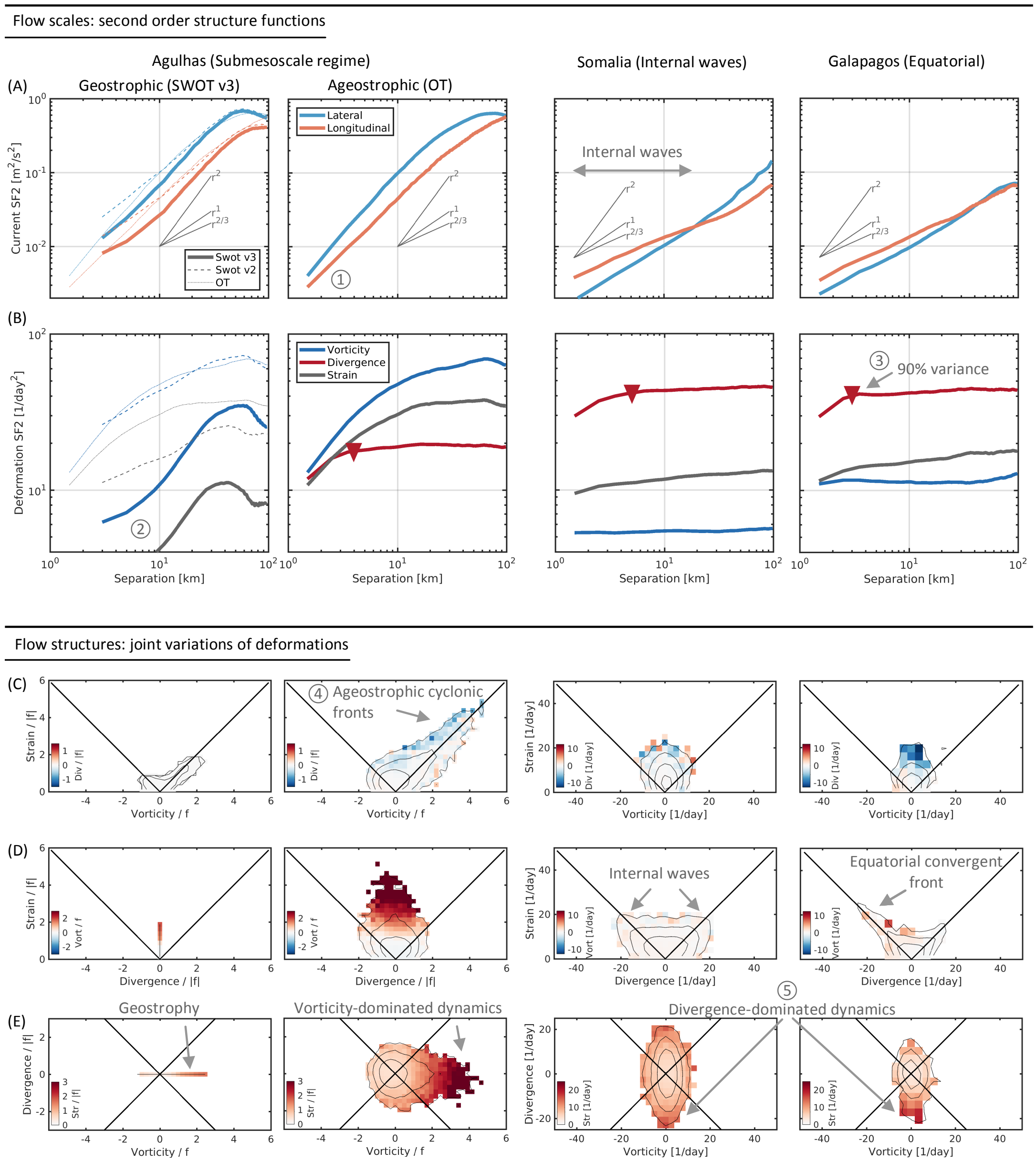

Fig. 3 **Beyond geostrophy: OT reveals flow scales and coherent structures across submesoscale, internal-wave and equatorial dynamical regimes.** Scales are characterized by the second-order structure functions of currents **(a)** and of vorticity, strain and divergence **(b)**. Red triangles indicate the scale below which 90% of the divergence variance occurs. Structures are characterized by the joint variations of deformations **(c-e)**; for instance, in panel (c), contours show the joint PDF of vorticity and strain, while colors show divergence conditioned on vorticity and strain. Compared to geostrophy, OT resolves finer flow scales ① and enhanced strain variability ②, while revealing a strong concentration of divergence at scales below 5 km ③. Divergent and ageostrophic structures emerged both within the vorticity-dominated submesoscale regime ④ and in regimes where divergence dominates over vorticity ⑤. Additional dynamical regimes are shown in Extended fig 3.

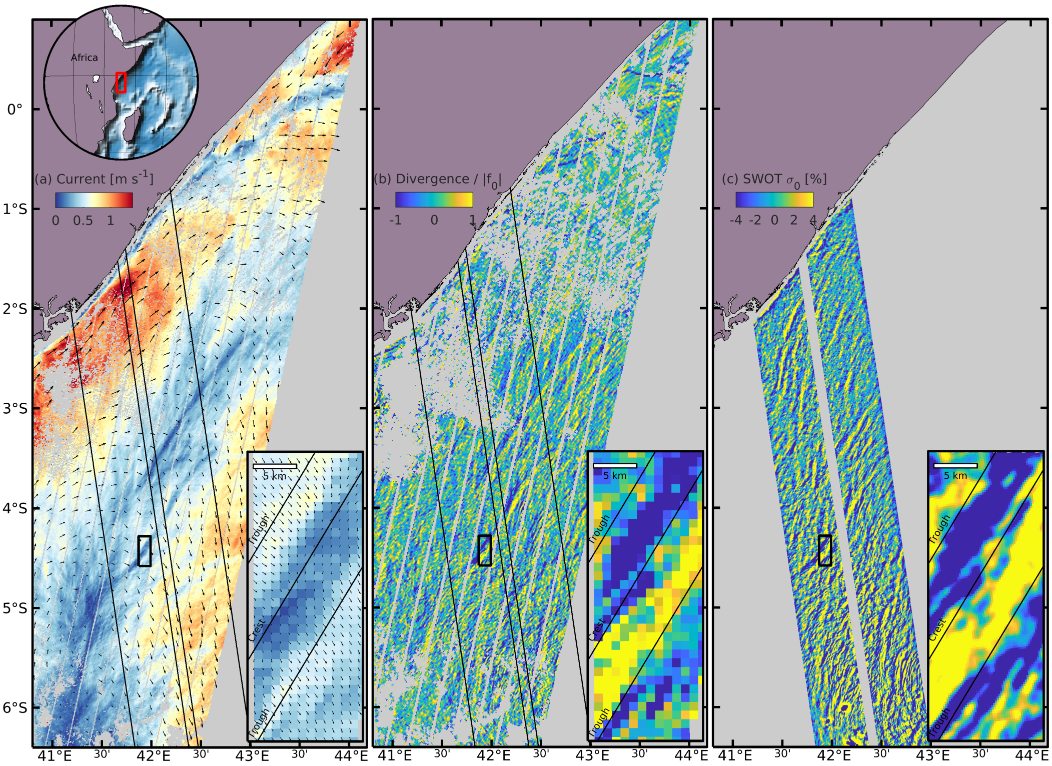

Fig. 4 Equatorial and internal wave currents off Somalia. (A,B) Currents derived from OT on 12 Dec 2024 at 07:40 UTC. **(a)** Current magnitude at 1 km resolution with vectors downsampled to 15 km for readability. The globe inset shows the wider regional setting with bathymetry. The inset highlights an internal wave packet, with vectors plotted at full resolution and SWOT SSH-derived crests and troughs shown for reference. **(b)** Current divergence, normalized by $f_0 = 10^{-4}$ s^{-1}. **(c)** Normalized radar cross section σ_0 observed by SWOT 9 minutes later (07:49 UTC), band-pass filtered to $1-10$ km and expressed as percent contrast to the background. Independently observed divergence and σ_0 show a close spatial match. Additional OT vorticity, SWOT SSH and model data are shown in Extended fig 4.

vanishes at these latitudes. This is illustrated by current observations along the Somalia and Kenya coastlines (Fig. 4). At large scales, two coastal jets form an equatorial confluence ($0° - 1°$S), characteristic of the winter monsoon in the Somali Current and in agreement with numerical models (Extended fig 4a). This case demonstrates that OT observes equatorial currents as effectively as currents elsewhere.

At fine scales, in the southern part of the region ($3° - 6°$S), the current appears disorganized, with a branching, arborescent texture, weak vorticity, and much stronger divergence, forming a dense web of intertwined bands (Fig. 4b and Extended fig 4b). This puzzling organization –in stark contrast to the Agulhas region– may at first raise doubts about the accuracy of the OT current field. However, the SWOT satellite passed over the same region nine minutes later, and its radar cross section σ_0, which reflects current gradients through wave roughness modulation (Method 3), provides a decisive validation of the divergence patterns down to the finest details (correlation of 0.75 over 10^5 ocean samples; Fig. 4c). This is a remarkable agreement for a first direct satellite observation of divergence. In particular, a momentum balance analysis (Method 3) confirms that the apparent web arises from a rarely observed current regime: an ocean teemed with internal waves. Internal waves are routinely observed in radar σ_0 and, more recently, in swath altimetry through their SSH imprint. Yet estimating currents from these indirect measurements requires additional information on stratification, assumptions about vertical modes, and disentanglement from balanced currents[26,52]. Here, the current field is directly observed and, when collocated with SSH observations, provides strong constraints on internal-wave dynamics and vertical structure (Method 3).

Beyond these expected signatures of internal waves, the observations reveal the structure of equatorial fronts – much less documented than their Coriolis-balanced mid-latitude counterparts[53–55]. The Somali equatorial confluence ($0° - 1°$S) emerges as multiple sharp, kilometre-wide convergent lines with strong anticyclonic vorticity (reversing sign across the equator, positive south and negative north, Extended fig 4). In another equatorial scene near the Galapagos Islands, associated with the trailing edge of a Tropical Instability Wave, similar sharp convergent fronts (indicated by the magenta arrows, Extended fig 5) are observed. These fronts exhibit either cyclonic vorticity or the weak vorticity expected as they transition into gravity-current fronts[53], but at times also anticyclonic vorticity (middle magenta arrow), suggesting a complex dynamical interplay with the synoptic circulation. The joint distributions of vorticity, strain and divergence further highlight the peculiarities of this equatorial regime: convergent fronts characterized by large divergence-strain signatures depart markedly from the vorticity-strain dominated mid-latitude fronts observed in the Agulhas (Fig. 3d,e). Internal waves also stand out through a symmetric heart-shaped strain-divergence distribution. Their interplay with fronts –otherwise entangled in altimetric SSH measurements– should be directly accessible with the present observations.

More broadly, these satellite observations demonstrate an observational shift beyond the predominantly geostrophic regime, providing direct access to dynamical regimes in which divergence becomes comparable to, or even exceeds, vorticity (Fig. 3e and Extended fig 3e).

Coastal currents

In a third case study, OT captures a coastal current that is elusive to altimetry. The example appears off southwestern Madagascar, with quasi-simultaneous OT and SWOT observations only 48 min apart (Fig. 5). Just northeast of a submesoscale spiraling cyclone – forming a characteristic "cat's eye" structure[1,3,56] – OT captures a powerful southeastward coastal jet, reaching 1.1 m s^{-1} and nearly 40 km wide. A wider composite including the adjacent OT swath three days later reveals the full extent of the jet along the Madagascar coast (Extended fig 6a). This major poleward current – recently identified from shipborne surveys as the Southwest Madagascar Coastal Current (SMACC)[57] – has long been known locally yet remains barely visible to altimetry. Here traditional altimetry underestimates it by 70% (Extended fig 6c, 0.3 m s^{-1}), and

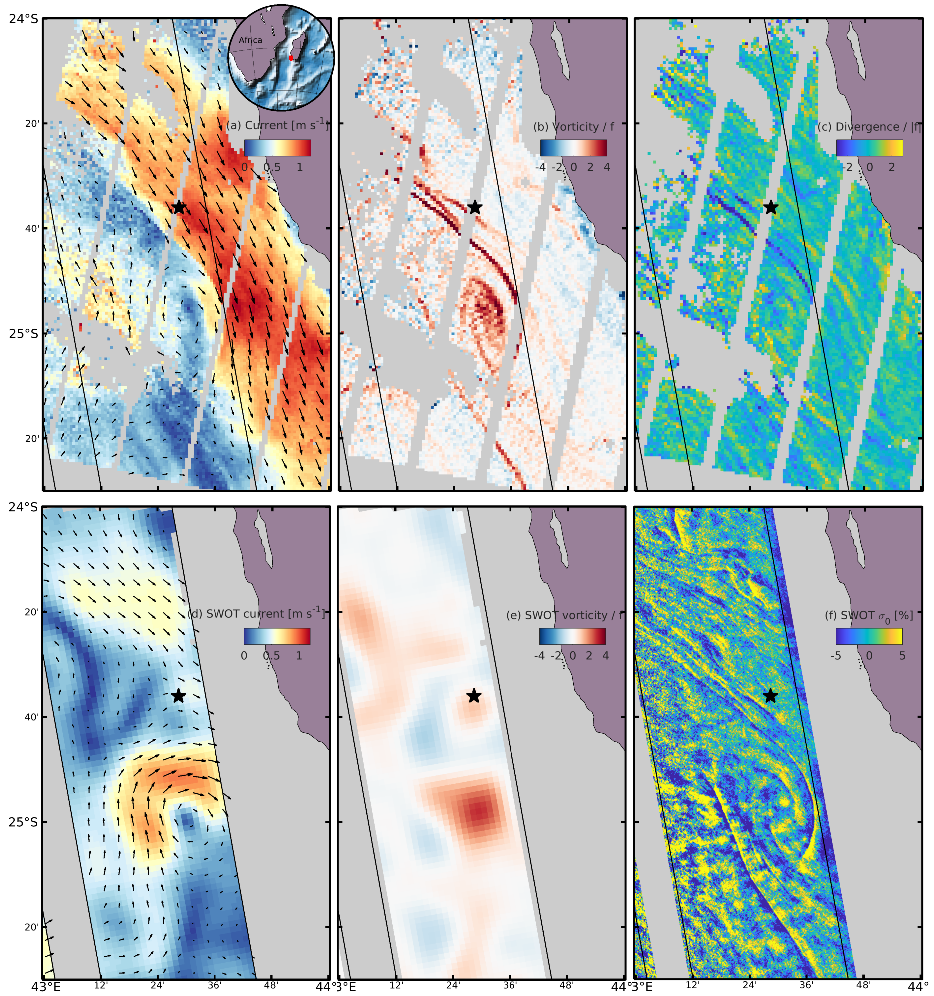

Fig. 5 Coastal jet off Madagascar. OT images the recently identified Southwest Madagascar Coastal Current and a "cat's eye" submesoscale cyclone, proposing improvements for swath altimetry currents.**(a-c)** Current, vorticity and divergence derived from OT on 13 Dec 2024 at 07:18 UTC. Missing data correspond to clouds and areas where surface waves were too weak to track. **(d-f)** Geostrophic current, geostrophic vorticity and σ_0 contrast observed by SWOT 38 minutes later (07:56 UTC). A black star marks the location where mean sea level correction using OT should help SWOT to capture the coastal jet. To ease the comparison, the SWOT swath (current field, slightly narrower than the σ_0 field) is outlined on each panel. Vectors are downsampled to 6 km for readability. A wider view of the Madagascar current system is shown in Extended fig 6.

even the latest SWOT swath data capture only discontinuous fragments with local underestimations by 60% (black star in Fig. 5d, 0.4 m s^{-1}).

This fragmented representation in altimetric observations is puzzling: as a large current far from the equator, it must be in geostrophic balance and should imprint clearly on sea level. The most likely explanation is an error in the mean dynamic topography: without historical drifter constraints, the coastal sea-level slope associated with the geostrophic current becomes indistinguishable from a static gravity anomaly [58–60]. How many other coastal currents escape satellite detection? OT observations could help address this structural limitation of altimetry, providing direct velocity constraints for a more accurate mean dynamic topography across undersampled coastal regions worldwide.

Implications

This work introduces a new approach to directly image ocean surface currents from space at kilometre scale. This new capability is demonstrated opportunistically during Sentinel-2 calibration phases, and the relatively simple tandem configuration of generic optical sensors offers a scalable approach for future dedicated satellite missions.

Although limited to cloudless and favorable observing conditions, the retrieval method is direct and calibration-free – requiring neither geostrophic assumptions nor geophysical model functions – and therefore provides an independent reference to validate and complement other current retrieval techniques based on radar, altimetry or machine learning. Systematic comparison with numerical simulations will provide observational constraints to improve model physics and calibration.

These first direct images of ocean currents shift satellite observations beyond the predominantly geostrophic regime, revealing submesoscale, internal-wave, coastal and equatorial dynamics. More than a proof of concept, they expose the characteristic flow scales and coherent structures across these diverse regimes. The observed concentration of divergence at scales below 5 km, previously unresolved from space, points to intense fine-scale vertical motions that remain poorly constrained by existing upper-ocean observations and models.

For decades, satellites have measured temperature, color and roughness, and more recently winds and waves, yet lacked high-resolution surface currents. This missing variable has limited our understanding of ocean surface layer dynamics, coupled ocean–wave–atmosphere processes, and their role in ocean transport and biogeochemical pathways. By providing direct kilometre-scale measurements of surface currents, this work opens a new observational window onto the multiscale physics of the upper ocean and its role in Earth's climate system.

MATERIAL

Sentinel-2 optical tandem phases

We use 10 m resolution optical images from Sentinel-2, a satellite mission designed primarily for terrestrial applications and mainly covering coastal ocean regions[61]. A single satellite routinely provides image pairs separated by about 1 s because the band detectors are tilted with respect to the nadir plane[62]. Here, we opportunistically leverage calibration phases of the Sentinel-2 constellation – S2A and S2C (Oct-Dec 2024) and S2A and S2B (Feb 2026) – during which two satellites were flown in tandem along the same orbit approximately 27.4 s apart (Fig. 1).

Observational availability

The ability to retrieve the surface current depends on both environmental and observational conditions. The presence of wind waves, with sufficiently broad directional and wavelength distributions, is essential (see Method 1). Given the Nyquist frequency of Sentinel-2 sensors at 20 m, this requirement excludes calm conditions with wind speeds below about 5 to 6 m s^{-1}. A criterion based on the number of coherent wave components is used to reject unreliable current estimates in low-wind regions, such as the northwestern part of the Madagascar area (Fig. 5). A high Sun elevation also improves the signal-to-noise ratio, favoring summer conditions and sunglint geometries over winter periods with low solar angles, when the brightness modulation induced by surface waves often falls below the detection threshold.

The Sentinel-2 tandem phase represents an opportunistic proof of concept for this method. A future dedicated mission, designed with higher horizontal resolution, optimized viewing geometry, and improved signal-to-noise ratio, would provide significantly enhanced precision and spatial coverage, and is currently being prepared for proposal.

METHOD 1: Current retrieval from wave phase shift

Theoretical wave phase and current-induced shift

For a monochromatic wave propagating in deep water in the direction of the wavevector $\vec{k}$, its phase can be written as

$$\Phi = \vec{k}.\,(\vec{x} - \vec{u}t) - \sqrt{gk}\;t, \tag{1}$$

where k is the wavenumber, $\vec{u}$ the underlying current, and the deep-water dispersion relation has been used.

The phase difference between two instants separated by Δt is then

$$\Delta\Phi = -\sqrt{gk}\;\Delta t - \vec{k}.\vec{u}\Delta t, \tag{2}$$

where the last term represents the current-induced phase shift.

If $\Delta\Phi$ is observed for a given wavenumber k, this relation in principle enables retrieval of the current component along the direction of $\vec{k}$. Two ambiguities, however, prevent a direct inversion: (i) the phase is wrapped modulo 2π, and (ii) the wave propagation direction has a 180° ambiguity. Explicitly,

$$\frac{\vec{k}}{k}.\vec{u} = -\frac{\Delta\Phi + n2\pi}{k\Delta t} \pm \sqrt{\frac{g}{k}}, \tag{3}$$

where the $\pm$ sign accounts for the directional ambiguity and n is an integer accounting for the phase wrapping.

For a typical wind wave of wavelength ~ 60 m and a time lag ~ 3 s, the ambiguities are irrelevant since $2\pi/(k\Delta t)$ corresponds to a velocity of about 20 m s^{-1}, unrealistic for ocean currents. For the Sentinel-2 OT configuration with a 30 s time lag, the ambiguities corresponds to 2 m s^{-1}, comparable to the Agulhas Current velocity. These ambiguities can only be resolved by combining phase shifts from multiple wave components with different wavenumbers.

Observed cross spectrum coherence

To compute the current from an optical image pair, we extract a square box where waves are clearly detected (Fig. 1a). First the cross-spectrum is computed following the Welsh method[63],

$$\hat{I}_{12}(\vec{k}) =< \hat{I}_1^* \hat{I}_2 >, \tag{4}$$

where $<>$ denotes an average over sub-images that are twice smaller, Hann filtered and half overlapping. An indication of the phase noise of the cross spectrum is given by the coherence spectrum ($0 \leq C \leq 1$), defined as[42,64]

$$C_{12}(\vec{k}) = \frac{\left| < \hat{I}_1^* \hat{I}_2 > \right|}{\sqrt{< \hat{I}_1^* \hat{I}_1 >< \hat{I}_2^* \hat{I}_2 >}}, \tag{5}$$

and corresponding to the square root of the magnitude-squared coherence[43,65].

For OT image pairs separated by 30 s, the coherence typically ranges between 0.5 and 0.7 (Fig. 1b). Although these values are lower than those obtained for short-delay image pairs (1 s), where coherence usually reaches 0.8-0.9[42,43], they remain remarkably high. This indicates that the phase noise on short wind waves remains low even after such long time lags.

This property is central to this study. Provided that the phase can be unwrapped, as discussed below, the long time lag is highly beneficial: it reduces the noise on the current estimate, despite a slightly higher phase noise caused by the partial loss of coherence (see eq. 3). This balance between increased phase noise and longer time separation, well known for Doppler radar design[66,67], suggest a surprisingly long optimal time lag, on the order of tens of seconds rather than the few milliseconds encountered for radars.

Observed phase shift and current retrieval

The theoretical framework (eq. 2) provides the following relationship between the observed phase shift and the underlying current:

$$\arg\left[< \hat{I}_{12} > \exp(i\sqrt{gk}\ \Delta t)\right] = \arg\left[\exp(-i\vec{k}.\vec{u}\Delta t)\right], \tag{6}$$

which holds for all wavevectors $\vec{k}$.

The current retrieval proceeds in three deterministic steps. First, wave components with coherence $C(k) < 0.5$ are discarded (Fig. 1c,d). Second, the 180° propagation ambiguity is removed using the phase difference at short time lags (1 s)[68]. Third, phase wrapping, which allows for an infinite number of current solutions for a given wavenumber k, is resolved by seeking a global fit to eq. 6 (Fig. 1e,f) using the circular cost function

$$Cost(\vec{u}) = \sum_{C(k)>0.5} \left|\exp i\phi_{obs} - \exp i\phi_{mod}\right|^2, \tag{7}$$

with ϕ_{obs} and ϕ_{mod} respectively the lhs and rhs of eq. 6.

This inversion of the dispersion relation does not involve statistical parameterizations, learning-based models, or empirical calibration of the phase-current relationship. It is a direct physics-based current retrieval, fully anchored in linear wave theory.

Current sampling depth

When the current exhibits vertical shear, the effective sampling depth of the waves scales with their wavelength[69]. The wind-waves used in here, with wavelengths of $30-150$ m, therefore sense currents at depths of approximately $\simeq 2-12$ m, assuming a constant vertical shear[70]. In the minimization procedure to retrieve the current from eq. 6, vertical shear has not been considered and is left for future studies.

Horizontal resolution

The surface current is computed over independent 1.3-km boxes with a 1-km posting. Each box is divided into nine overlapping sub-images, twice smaller and shifted by half their size[63]. The averaged phase shifts give four times more weight to the box center than to its corners, yielding an effective resolution of about 1 km. A higher-resolution (500 m) processing tested for the Agulhas case revealed finer-scale structures but also more noise.

METHOD 2: OT current validation and uncertainty

Validation of the OT current field at 1 km resolution is conducted using a two-scale approach. The first level assesses large-scale accuracy and consistency with other current measurements, evaluating patterns, magnitude and direction. The second level focuses on small-scale precision through validation of current gradients. Finally, uncertainty is estimated internally from the phase noise.

Large-scale current accuracy

In the Agulhas case, the current location, magnitude and direction closely align with those identified in the nearest SWOT observations collected 12 hours earlier (correlation of 0.92 over 2931 samples, Extended fig 2e,f). SWOT velocities exceed OT by approximately 0.2 m s^{-1}. Several factors may account for this difference: the temporal offset between the observations, the geostrophic approximation underlying the SWOT current retrieval, and the presence of a wind-driven surface current (northeastward wind) not captured by SWOT. Additional comparisons with HF radars over the Agulhas Current on 14 Dec 2024 (not shown) and 22 Feb 2026 (fig Extended fig 7) show similarly good agreement (correlations of 0.9 over 525 samples).

In the Somali current region, altimetry does not provide reliable measurements due to the equatorial proximity, but the OT patterns show qualitative agreement with numerical simulations for this area (Extended fig 4a).

Lastly, very few surface drifters are available in coastal regions, but the limited collocations show similar agreement, with differences of the order of $0.1 - 0.2$ m s^{-1} for each velocity component (not shown).

Current gradient validation

Beyond these large-scale comparisons, the current gradients provide a compelling demonstration of the precision of the retrieved velocity field. Gradient locations exhibit sharp spatial correspondence with fronts detected independently by multiple satellites, using diverse sensors and physical contrast mechanisms (superimposable panels are provided in the Data S1). For instance, in the Agulhas case, 80% of current fronts –defined as the 5% strongest magnitude of the velocity gradient tensor – lie within 3 km of a SST sea surface temperature front (observed by Sentinel-3, Fig. 2d), whereas only 18% would be expected under random translations of the current field (Monte Carlo test, 10 000 realizations, p = 0.0013).

Such sharp spatial agreement is also observed with the equatorial Pacific temperature front (Sentinel-3, Extended fig 5), with ocean color fronts around New Zealand (Sentinel-2, Extended fig 1) and with surface roughness fronts associated with the South Madagascar Coastal Current and the Pacific equatorial front (SWOT, Fig. 5 and Extended fig 5).

The most compelling validation is provided by SWOT observations of internal waves off Somalia (Fig. 4b,c). The physical mechanism is explained in Method 3. OT divergence closely corresponds to SWOT σ_0 down to the finest scales (Fig. 4b,c), with a correlation of 0.75 over 10^5 ocean samples – a remarkable agreement for such higher order physical variable, directly observed from space for the first time.

Current accuracy and precision

The current accuracy is mainly related to georeferencing accuracy. In the first Sentinel-2 OT data release, co-registration errors of up to one pixel were present in both along-track and across-track directions, corresponding to current errors of up to 30 cm s^{-1}. These shifts can be estimated over land using a modified cost function with no wave propagation (no term $\exp(i\sqrt{gk}\ \Delta t$ in eq. 6). They exhibit long spatial wavelengths, and can thus be corrected for ocean scenes using nearby land as ground control points to remain below 10 cm s^{-1}. While such errors affect absolute current values, they do not impact current precision and thus gradients at meso and submesoscales.

The current precision can be estimated internally under the assumption of Gaussian noise in the independent wave phase shifts, yielding to a current covariance $Cov = 2\sigma^2 H^{-1}$, where σ^2 is the observed variance of the residual phase (eq. 6), and H is the Hessian of the cost function (eq. 7). Under favorable conditions, more than 100 phase shifts with coherence greater than 0.5 (Fig. 1B) are typically available. This suggests precision better than 0.5 cm s^{-1} along the main wave direction (downwind), and about 1.5 cm s^{-1} in the crosswind direction for cases with a broad directional wind-wave spectrum (Fig. 1E). In some regions, the precision degrades to $5 - 10$ cm s^{-1}, particularly in the crosswind direction, most likely due to a reduced directional spreading of coherent waves (Extended fig 8b). These internal precision estimates are consistent with observed structure functions of currents at small spatial scales (Fig. 3a), which suggest precision about 4 cm s^{-1} (Method 4).

Assuming independent neighbouring cells, a velocity precision of 1 cm s^{-1} implies a current-gradient precision of 1.4×10^{-5} s^{-1} over 1 km (approximately 0.14 f at mid-latitudes) and 1.4×10^{-6} s^{-1} over 10 km (approximately 0.014 f at mid-latitudes).

METHOD 3: Internal waves observed by OT and SWOT

SWOT measures both sea surface height (SSH) and the normalized radar cross section σ_0, which represents radar return intensity and has long been known to reflect current gradients through wave-current interactions[71,72]. When an internal wave propagates near the surface, the SSH crest is preceded by convergence which steepens short wind waves, thereby roughening the ocean surface and reducing σ_0. Behind the crest, the opposite occurs: divergence smooths the surface[52,71].

In the Somalia case (Fig. 4 and Extended fig 4), we find strong agreement between OT divergence and SWOT σ_0 (correlation of 0.75 over 10^5 samples), together with the phase quadrature with SSH consistent with internal waves propagating northwestward (see insets).

Another line of evidence for internal wave dynamics comes from a momentum balance consideration: the pressure gradient force, computed from SWOT SSH as $g\nabla SSH$ (with g the gravitational acceleration), exceeds the advection term and the Coriolis force by one and two orders of magnitude, respectively, both estimated from OT as $u \cdot \nabla u$ and fu (with u the current).

In previous studies, internal waves have been observed from space using two main approaches. The first exploits σ_0, which is inverted into current gradients using external information on wind and wave conditions, together with approximations of wave–current interactions and radar imaging mechanisms[55,73]. The second uses SSH, from which currents are inferred under assumptions on background stratification and internal-wave vertical modes[52,74]. Both approaches suffer from entanglement with balanced (i.e. non–internal-wave) currents.

The direct detection method of OT bypasses these limitations, opening new possibilities to investigate interactions between internal waves and complex currents.

Furthermore, new capabilities arise for a more precise dynamical characterisation of internal waves when SSH and OT are simultaneously observed, as illustrated in the Somalia case. Assuming linear dynamics, a first estimate of the phase speed $c = g \cdot SSH/u$ yields about 1 m s^{-1}. A second, independent estimate based on the 390 m phase displacement observed over the 9-minute separation between SWOT σ_0 and OT divergence gives a phase speed of about 0.7 m s^{-1}. Accounting for a mean opposing current of 0.6 m s^{-1} yields an intrinsic phase speed of about 1.3 m s^{-1} (assuming a barotropic background flow). Hydrographic vertical profiles suggest phase speeds of 2.1 m s^{-1} and 1.3 m s^{-1} for mode-1 and mode-2 internal waves, respectively. The estimates are therefore broadly comparable in magnitude, while the remaining discrepancies may reflect nonlinear wave dynamics, uncertainties in stratification, or the influence of background baroclinic flows. Together, it demonstrates the added value of direct current measurements in disentangling internal-wave signals from balanced motions and in constraining their dynamical properties. This points towards the need for systematic investigations of internal-wave dynamics across diverse oceanic regimes using collocated velocity, SSH, and radar observations.

METHOD 4: Flow deformation properties and scale distribution

Current vorticity, divergence, and strain

The spatial deformations of the horizontal current field with components (u, v) oriented along the eastward (x) and northward (y) axes may be decomposed into four standard fields: relative vorticity $\xi = \partial v/\partial x - \partial u/\partial y$, horizontal divergence $\delta = \partial u/\partial x + \partial v/\partial y$, normal strain $\sigma_n = \partial u/\partial x - \partial v/\partial y$, the shear strain $\sigma_s = \partial v/\partial x + \partial u/\partial y$. Vorticity and divergence are invariant under rotations of the coordinate system, while individual strain components are not, which classically motivates the use of total strain $\sigma = \sqrt{\sigma_n^2 + \sigma_s^2}$ instead.

Deformation fields are computed directly from the retrieved current field using centered finite differences on three-point stencils.

Structure functions

Second order structure functions quantify the characteristic amplitude of spatial increments of a variable θ over a separation distance r:

$$S_\theta(r) = \langle \left[\theta(\mathbf{x}') - \theta(\mathbf{x})\right]^2 \rangle_{||\mathbf{x}-\mathbf{x}'||=r}. \tag{8}$$

In this study, θ denotes either the velocity, decomposed into along-separation velocity component $u_\parallel$, which yields the longitudinal structure function, and the across-separation component $u_\perp$, which yields the lateral structure function, or deformation fields such as vorticity, divergence, and strain. Structure functions asymptote to twice the variance of the variable when separation distances exceed its characteristic spatial scales - scales over which the field gets spatially decorrelated. At smaller separation, second-order structure functions reflect the distribution of energy across scales and are related to power density spectra via cosine transforms[75,76]. This results in a heuristic relationship – a power density spectrum following a power law k^{-n} with $1 < n < 3$ corresponds to a structure function scaling as r^{n-1}. Unlike standard power spectral analysis, the computation of structure functions does not require regularly gridded data, which is a clear advantage given the presence of gaps in the OT fields. Structure functions have previously been estimated from in-situ observations of currents collected from moving platforms such as ships[77], gliders[78], and moorings[79]. Surface drifters have also been used[80], but systematic biases associated with their convergence and divergent trajectories complicate their interpretation[81]. A common objective in past efforts has been to quantify the rotational and divergent flow contributions across scales[82], which can provide insights into the flow dynamics (e.g. geostrophically balanced flows are primarily rotational). However, doing so generally requires assumptions such as isotropy and homogeneity, followed by inversion of expected theoretical relationships (see[83] for alternative propositions). Here, we bypass these assumptions and take an alternative approach by directly computing structure functions of flow-deformation variables to infer dynamical signatures, enabled by the high resolution and low noise of the OT current field.

In the observed flow structure functions (Fig. 3a), the absence of near-origin flattening suggests that the instrumental noise floor has not yet been reached. In the Agulhas case, this implies velocity error smaller than $\sqrt{0.003/2} \simeq 4$ cm s^{-1}, consistent with independent estimates from wave phase noise.

In the Agulhas region, flow structure functions are consistent with expectations for balanced oceanic turbulence (Fig. 3a). More specifically, their slopes lie between r^1 and $r^{1.5}$, and the lateral structure function exceeds the longitudinal one by a factor consistent with the observed slope[80]. In the New Zealand, Somalia and Galapagos cases (Fig. 3a and Extended fig 3a), internal waves produce shallower slopes, between $r^{2/3}$ and r^1, particularly for the longitudinal component. In the Somalia region, the relative magnitude of the longitudinal and lateral structure functions further reveals a transition in the dominant dynamics across scales: divergent motions associated with internal waves dominate below about 20 km, while balanced vortical motions dominate at larger scales.

The most recent observations from airborne Doppler radar[51] suggest even shallower slopes in the 1-10 km range (Extended fig 3a). Sophisticated wave-current coupled models generating Langmuir cells have been proposed to reproduce such enhanced small-scale variability. The absence of comparable variability in the OT observations is therefore puzzling, particularly given the energetic wave conditions (4 m significant wave height) encountered in the Agulhas case.

OT also provides unique insight into the scale distribution of flow deformation fields through their structure functions (Fig. 3b and Extended fig 3b), which further confirm the low noise levels even for these higher-order quantities. In the Agulhas case, the weakly divergent nature of the flow is apparent, whereas divergence is more energetic in the other regions.

Across all regimes, divergence is concentrated at scales finer than 5 km, which contain 90% of its variance (red triangles), as indicated by the plateau reached at larger separations. This concentration at kilometre scales likely reflects contributions from both frontal dynamics and internal waves. Although their respective contributions cannot be readily separated, frontal dynamics appear to dominate a substantial fraction of the most energetic divergence events. For instance in the Agulhas case, the 5% strongest divergence pixels - which account for 40% of the total divergence variance despite occupying only 5% of the surface - are not randomly distributed: 39% occur within 3 km of the 5% strongest SST gradients, compared with only 19% expected under random translations (Monte Carlo test, 10 000 realizations, p=0.038). This preferential clustering indicates that frontal dynamics are an important contributor to the observed kilometre-scale divergence, alongside internal waves. These direct observations support longstanding hypotheses that kilometre-scale processes play a central role in upper-ocean vertical exchange and imply stringent spatial-resolution requirements for both satellite observations and numerical models aiming to resolve it.

Lastly, the vorticity and strain structure functions in the Agulhas case continue to increase up to scales of about 20 km, indicating that these fields remain spatially coherent over larger scales than divergence. In comparison, two versions of SWOT level 3 geostrophic flows are examined, the v2 (shown in Extended fig 2c) and the more horizontally smoothed v3. Both exhibit structure functions consistent with the OT estimates at large scales, while instrumental noise produces a mild flattening at separations smaller than 10 km (Fig. 3a and Extended fig 3a). SWOT v3 displays substantially reduced variability below 30 km scales. In contrast, the SWOT v2 vorticity structure function closely matches the OT counterpart, whereas its strain structure function amplitude is reduced by roughly a factor of two, indicating a substantial underestimation of strain variance (Fig. 3b and Extended fig 3b).

Joint distributions of flow deformation fields

Joint probability distributions of deformation fields are widely used to identify oceanic dynamical regimes[16,23,49,84]. In the Agulhas case, the averaged divergence conditioned on vorticity and strain provides a rare observational confirmation of high-resolution numerical predictions for balanced oceanic turbulence[49]. In particular, the distribution exhibits strong cyclonic skewness, with clustering along the line of equal strain and vorticity at large amplitudes and enhanced convergence in regions of high strain (Fig. 3c). Such analyses are largely out of reach for altimetry: divergence is not directly available from altimetry observations, and the vorticity-strain distribution is itself distorted by geostrophic assumptions[23]. Here, vorticity-strain distributions from SWOT v2 and SWOT v3 are shown for the Agulhas case, and exhibit a markedly reduced cyclonic skewness, particularly for the v2 product (Fig. 3c and Extended fig 3c).

In the Somalia region, the cyclonic skewness disappears and a heart-shaped pattern emerges in the strain-divergence joint probability distribution (Fig. 3d). Such a pattern is theoretically expected in internal-wave-dominated flows[23] and has only recently been identified in HF radar measurements[84]. Equatorial dynamics also exhibit characteristic signatures. The Galapagos equatorial front is marked by strong convergence and strain despite weak vorticity (Fig. 3c,d), whereas the Somalia equatorial confluence exhibits anticyclonic convergent structures (Extended fig 3c,d).

The divergence-vorticity joint distributions (Fig. 3e and Extended fig 3e) highlight the observational shift beyond geostrophic dynamics: OT reveals flow regimes dominated by divergence rather than vorticity, as well as mixed dynamics (for example the New Zealand case and the Somalia equatorial confluence).

METHOD 5: Comparisons with state-of-the-art numerical simulations

Comparison with numerical simulations provides context to OT observations. Such comparisons can be performed with realistic analysis of the exact conditions encountered (here using CMEMS global_analysisforecast_phy_001_024 available at https://doi.org/10.48670/moi-00016). Examples are shown in Extended fig 4a and Extended fig 6f. The main caveats are the reduced resolution (1°/12) and the fact that the dynamics are influenced by assimilation of a broad range of observations, including altimetry. Free model runs at higher resolution do not suffer these limitations and are therefore also insightful. These are performed with the widely used MITgcm LLC4320[85] and the CROCO regional model[47]. True comparisons with such free numerical simulations will only be possible statistically once months of OT data have accumulated. Nonetheless qualitative comparisons with year-long simulations provide a sense of the likely outcome, and corresponding movies are provided (Movies S1 to S4).

At first glance, the level of realism of LLC4320 is remarkable, given the variety of dynamical regimes covered in this paper – from the strong Agulhas to internal waves and equatorial currents. This agreement is particularly noteworthy given the reduced effective resolution of the model and should provide strong motivation for the modelling community. A few clear differences can nonetheless be identified. Except of a few intense events, the South Madagascar Coastal Current is generally weaker in LLC4320 than observed by OT, suggesting that underestimation in CMEMS analyses primarily reflect a model bias than a bias induced by altimetry assimilation. Another notable difference appears in the core of the Agulhas Current, which is filled with bathymetric lee waves in all models, as evident in their divergence fields (see Movies S1 and S2 around 34.5°S 26°E).

These movies illustrate a notable shift: whereas observations of currents once lagged behind numerical models in resolution, OT now provides opportunities of quantitative comparisons.

Supplementary information. We provide an accompanying file containing all figures with separate, superimposable panels, enabling direct comparison of current, vorticity, temperature, and other fields for each scene discussed.

We also include four movies from state-of-the-art numerical simulations of discussed scenes to highlight model–observation differences (see Method 5).

Acknowledgements. We thank Luc Lenain for collaborations on the Doppvis airborne measurements, which gave additional motivation for the study, Alexandra Cuevas for her input on the Sentinel-2 data, Justin Stopa for his input on Sentinel-1 remote sensing, Julien Le Sommer for his input for community outreach, Shafer Smith, Nick Pizzo and Roy Barkan for their inputs on submesoscales, Hector Torres, Gerald Dibarboure and Solene Jousset for their input on SWOT remote sensing, Pierrick Penven and Jonathan Gula for their inputs on Madagascar currents and for the numerical simulation movies, Ferran Gascon and the Sentinel-2 team for helping with the tandem data, Sebastien Smet and the Actimar team for helping with the HF radar data, Delphine Hypolite for her input on DopplerScatt structure functions.

Declarations

- Funding:
  This work work supported by Consejo Nacional de Humanidades, Ciencias, y Tecnologías (CONAHCYT) through the project (2020-2023 contract CF2019-116328), by European Space Agency (ESA) through the projects Streamex (2023-2024) and IASCO (2021-2025, contract 4000129945/19/NL/FF/gp), by Centre National d'Etudes Spatial (CNES) through the project MASAIproof (2025-2028).
- Conflict of interest/Competing interests:
  The corresponding author declares that none of the authors has any competing interest.
- Processed data and code availability:
  Reaching the widest possible community is a key element of the scientific progress driven by these new observations. The data-sharing strategy will be threefold: (i) Processed surface current maps will be easily viewable through the online interface https://ovl.oceandatalab.com/, allowing straightforward collocation and overlay with other oceanographic datasets. (ii) The processed current maps will be distributed in NetCDF format. (iii) The full processing workflow will be released as open-source code on github, accompanied by a commented Jupyter notebook, enabling researchers to reprocess the data, explore regional refinements, and adapt the method to other data sources.
- Used data availability:
  All data used in the study are publicly available. The Sentinel-2 Level 1C are available from Copernicus website https://browser.dataspace.copernicus.eu. The Sentinel-3 SST data are available from Eumetsat website https://data.eumetsat.int. The SWOT Level-3 data[86] are available from Aviso website, https://tds-odatis.aviso.altimetry.fr/thredds/catalog/dataset-l3-swot-karin-nadir-validated/l3_lr_ssh/catalog.html, with the Unsmoothed σ_0 product at 250 m and the Expert filtered absolute geostrophic current product at

2 km at version v2.0.1 (Extended fig 2) and v3.0 (Fig. 5 and Extended fig 6). The CMEMS reanalysis global_analysisforecast_phy_001_024 are available from https://data.marine.copernicus.eu under https://doi.org/10.48670/moi-00016. The REMSS microwave SST data are available from https://data.remss.com/SST/daily/mw/v05.1/. The South Africa HF radar data are available from https://doi.org/10.15493/DEA.MIMS.20250406. The bathymetry data are from ETOPO1, a 1 arc-minute global ocean bathymetry by Amante, C. and B. W. Eakins, ETOPO1 1 Arc-Minute Global Relief Model: Procedures, Data Sources and Analysis. NOAA Technical Memorandum NESDIS NGDC-24, 19 pp, March 2009. The plots were done using Pawlowicz, R., 2020. "M_Map: A mapping package for MATLAB", version 1.4m, [Computer software], available online at https://www.eoas.ubc.ca/ rich/map.html. Additional color bars are taken from https://colorbrewer2.org.

- Author contribution:
  Conceptualization: NR, FN, RB, Methodology: NR, FN, FA, RB, FC, LM, Formal analysis and investigation: NR, AP, DB, BC, RA, LM, Data curation: RB, AP, NR, Writing – original draft: NR, Writing – review and editing: NR, AP, BC, FA, EB, RB, Visualization: NR, AP, Project administration and financing acquisition: NR, FA, LM.

References

[1] Scully-Power, P. Navy oceanographer shuttle observations, sts 41-g mission report. Tech. Rep., DTIC Document (1986).

[2] Yoder, J. A., Ackleson, S. G., Barber, R. T., Flament, P. & Balch, W. M. A line in the sea. *Nature* **371**, 689–692 (1994).

[3] Munk, W., Armi, L., Fischer, K. & Zachariasen, F. Spirals on the sea. *Phil. Trans. Roy. Soc. London A* **456**, 1217–1280 (2000).

[4] Hewitt, H., Fox-Kemper, B., Pearson, B., Roberts, M. & Klocke, D. The small scales of the ocean may hold the key to surprises. *Nature Climate Change* **12**, 496–499 (2022).

[5] Lévy, M., Franks, P. J. & Smith, K. S. The role of submesoscale currents in structuring marine ecosystems. *Nature communications* **9**, 4758 (2018).

[6] Schubert, R., Gula, J. & Biastoch, A. Submesoscale flows impact agulhas leakage in ocean simulations. *Communications Earth & Environment* **2**, 197 (2021).

[7] Mahadevan, A. The impact of submesoscale physics on primary productivity of plankton. *Annual Review of Marine Science* **8**, 161–184 (2016). URL https://doi.org/10.1146/annurev-marine-010814-015912. PMID: 26394203.

[8] D'Asaro, E. A. *et al.* Ocean convergence and the dispersion of flotsam. *Proceedings of the National Academy of Sciences* **115**, 1162–1167 (2018). URL http://www.

pnas.org/content/early/2018/01/09/1718453115.

[9] Su, Z., Wang, J., Klein, P., Thompson, A. F. & Menemenlis, D. Ocean submesoscales as a key component of the global heat budget. *Nature communications* **9**, 775 (2018).

[10] D'asaro, E., Lee, C., Rainville, L., Harcourt, R. & Thomas, L. Enhanced turbulence and energy dissipation at ocean fronts. *science* **332**, 318–322 (2011).

[11] McWilliams, J. C. Submesoscale currents in the ocean. *Proceedings of the Royal Society A: Mathematical, Physical and Engineering Sciences* **472**, 20160117 (2016).

[12] McWilliams, J. C. The nature and consequences of oceanic eddies. *Geophysical monograph series* **177**, 5–15 (2008).

[13] Chelton, D. B., Schlax, M. G. & Samelson, R. M. Global observations of nonlinear mesoscale eddies. *Progress in oceanography* **91**, 167–216 (2011).

[14] Klein, P. & Lapeyre, G. The Oceanic Vertical Pump Induced by Mesoscale and Submesoscale Turbulence. *Annu. Rev. of Marine Sci.* **1**, 351–375 (2009).

[15] Balwada, D., Smith, K. S. & Abernathey, R. Submesoscale vertical velocities enhance tracer subduction in an idealized antarctic circumpolar current. *Geophysical Research Letters* **45**, 9790–9802 (2018).

[16] Shcherbina, A. Y. *et al.* Statistics of vertical vorticity, divergence, and strain in a developed submesoscale turbulence field. *Geophysical Research Letters* **40**, 4706–4711 (2013).

[17] Farrar, J. T. *et al.* S-mode: the sub-mesoscale ocean dynamics experiment. *Bulletin of the American Meteorological Society* **106**, E657–E677 (2025).

[18] Fu, L.-L. *et al.* The surface water and ocean topography mission: A breakthrough in radar remote sensing of the ocean and land surface water. *Geophysical Research Letters* **51**, e2023GL107652 (2024).

[19] Chelton, D. B. A postlaunch update on the effects of instrumental measurement errors on swot estimates of sea surface height, velocity, and vorticity. *Journal of Atmospheric and Oceanic Technology* **41**, 865–888 (2024).

[20] Zhang, X. & Callies, J. Assessing submesoscale sea surface height signals from the swot mission. *Journal of Geophysical Research: Oceans* **130**, e2025JC022879 (2025).

[21] Tranchant, Y.-T., Legresy, B., Foppert, A., Pena-Molino, B. & Phillips, H. Swot reveals fine-scale balanced motions driving near-surface currents and dispersion in the antarctic circumpolar current. *Earth and Space Science* **12**, e2025EA004248

(2025).

[22] Archer, M., Wang, J., Klein, P., Dibarboure, G. & Fu, L.-L. Wide-swath satellite altimetry unveils global submesoscale ocean dynamics. *Nature* **640**, 691–696 (2025).

[23] Xiao, Q. *et al.* Reconstruction of surface kinematics from sea surface height using neural networks. *Journal of Advances in Modeling Earth Systems* **15**, e2023MS003709 (2023).

[24] Tréboutte, A. *et al.* Karin noise reduction using a convolutional neural network for the swot ocean products. *Remote Sensing* **15**, 2183 (2023).

[25] Torres, H. S. *et al.* Airborne observations of fast-evolving ocean submesoscale turbulence. *Communications Earth & Environment* **5**, 771 (2024).

[26] Gao, Z. *et al.* A deep learning approach to extract balanced motions from sea surface height snapshot. *Geophysical Research Letters* **51**, e2023GL106623 (2024).

[27] Gommenginger, C. *et al.* Seastar: a mission to study ocean submesoscale dynamics and small-scale atmosphere-ocean processes in coastal, shelf and polar seas. *Frontiers in Marine Science* **6**, 457 (2019).

[28] Wineteer, A., Torres, H. S. & Rodriguez, E. On the surface current measurement capabilities of spaceborne doppler scatterometry. *Geophysical Research Letters* **47**, e2020GL090116 (2020).

[29] Chapron, B., Collard, F. & Ardhuin, F. Direct measurements of ocean surface velocity from space: Interpretation and validation. *J. Geophys. Res* **110** (2005).

[30] Krug, M., Mouche, A., Collard, F., Johannessen, J. & Chapron, B. Mapping the agulhas current from space: An assessment of asar surface current velocities. *Journal of Geophysical Research: Oceans* **115** (2010).

[31] Marié, L. *et al.* Measuring ocean total surface current velocity with the kuros and karadoc airborne near-nadir doppler radars: a multi-scale analysis in preparation for the skim mission. *Ocean Science* **16**, 1399–1429 (2020).

[32] Fan, S., Kudryavtsev, V., Yurovsky, Y. & Zhang, B. Reconstructing ocean surface current vector field from sar doppler shift measurements. *Remote Sensing of Environment* **328**, 114855 (2025).

[33] Lenain, L., Srinivasan, K., Barkan, R. & Pizzo, N. An unprecedented view of ocean currents from geostationary satellites. *Nature Geoscience* 1–8 (2026).

[34] Uchida, T. *et al.* Cloud-based framework for inter-comparing submesoscale permitting realistic ocean models. *Geoscientific Model Development Discussions* **2022**, 1–32 (2022).

[35] Matthews, J. Stereo observation of lakes and coastal zones using aster imagery. *Remote sensing of environment* **99**, 16–30 (2005).

[36] Matthews, J. P. & Yoshikawa, Y. Synergistic surface current mapping by space-borne stereo imaging and coastal hf radar. *Geophysical Research Letters* **39** (2012).

[37] Laxague, N. J. *et al.* Observations of near-surface current shear help describe oceanic oil and plastic transport. *Geophysical Research Letters* **45**, 245–249 (2018).

[38] Stewart, R. H. & Joy, J. W. HF radio measurements of surface currents. *Deep Sea Research* **21**, 1039–1049 (1974).

[39] Lund, B. *et al.* Near-surface current mapping by shipboard marine x-band radar: A validation. *Journal of Atmospheric and Oceanic Technology* **35**, 1077–1090 (2018).

[40] Lenain, L. *et al.* Airborne remote sensing of upper-ocean and surface properties, currents and their gradients from meso to submesoscales. *Geophysical Research Letters* **50**, e2022GL102468 (2023).

[41] Kudryavtsev, V., Yurovskaya, M., Chapron, B., Collard, F. & Donlon, C. Sun glitter imagery of surface waves. part 2: Waves transformation on ocean currents. *Journal of Geophysical Research: Oceans* **122**, 1384–1399 (2017).

[42] Yurovskaya, M., Kudryavtsev, V., Chapron, B. & Collard, F. Ocean surface current retrieval from space: The sentinel-2 multispectral capabilities. *Remote sensing of Environment* **234**, 111468 (2019).

[43] Ardhuin, F., Alday, M. & Yurovskaya, M. Total surface current vector and shear from a sequence of satellite images: Effect of waves in opposite directions. *Journal of Geophysical Research: Oceans* **126**, e2021JC017342 (2021).

[44] Beal, L. M., Chereskin, T. K., Lenn, Y. D. & Elipot, S. The sources and mixing characteristics of the agulhas current. *Journal of physical oceanography* **36**, 2060–2074 (2006).

[45] Roberts, M., Van der Lingen, C., Whittle, C. & Van den Berg, M. Shelf currents, lee-trapped and transient eddies on the inshore boundary of the agulhas current, south africa: their relevance to the kwazulu-natal sardine run. *African Journal of Marine Science* **32**, 423–447 (2010).

[46] Krug, M., Swart, S. & Gula, J. Submesoscale cyclones in the agulhas current. *Geophysical Research Letters* **44**, 346–354 (2017).

[47] Tedesco, P., Gula, J., Ménesguen, C., Penven, P. & Krug, M. Generation of submesoscale frontal eddies in the agulhas current. *Journal of Geophysical Research: Oceans* **124**, 7606–7625 (2019).

[48] Bodner, A. S. *et al.* Modifying the mixed layer eddy parameterization to include frontogenesis arrest by boundary layer turbulence. *Journal of Physical Oceanography* **53**, 323–339 (2023).

[49] Balwada, D., Xiao, Q., Smith, S., Abernathey, R. & Gray, A. R. Vertical fluxes conditioned on vorticity and strain reveal submesoscale ventilation. *Journal of Physical Oceanography* **51**, 2883–2901 (2021).

[50] De Marez, C., Lahaye, N. J. & Gula, J. Interaction of the gulf stream with small scale topography: A focus on lee waves. *Scientific Reports* **10**, 2332 (2020).

[51] Hypolite, D. *et al.* Second-order velocity structure functions at submesoscales. *Journal of Physical Oceanography* **56**, 225–244 (2026).

[52] Siyahi, V. C., Chapron, B., Collard, F. *et al.* Internal waves observations from the surface water ocean topography mission: Combined sea surface height and roughness measurements. *ESS Open Archive* (2025).

[53] Warner, S. J. *et al.* Buoyant gravity currents released from tropical instability waves. *Journal of Physical Oceanography* **48**, 361–382 (2018).

[54] Pinkel, R. *et al.* Vertical momentum transport by internal gravity waves above the equatorial undercurrent at 140 w. *Geophysical Research Letters* **50**, e2022GL101630 (2023).

[55] Santos-Ferreira, A., Silva, J. d., St-Denis, B., Bourgault, D. & Maas, L. Internal solitary waves within the cold tongue of the equatorial pacific generated by buoyant gravity currents. *Journal of Physical Oceanography* **53**, 2419–2434 (2023).

[56] Ni, Q., Zhai, X., Wilson, C., Chen, C. & Chen, D. Submesoscale eddies in the south china sea. *Geophysical Research Letters* **48**, e2020GL091555 (2021). URL https://agupubs.onlinelibrary.wiley.com/doi/abs/10.1029/2020GL091555. E2020GL091555 2020GL091555.

[57] Ramanantsoa, J. D., Penven, P., Krug, M., Gula, J. & Rouault, M. Uncovering a new current: The southwest madagascar coastal current. *Geophysical Research Letters* **45**, 1930–1938 (2018).

[58] Rio, M., Guinehut, S. & Larnicol, G. New cnes-cls09 global mean dynamic topography computed from the combination of grace data, altimetry, and in situ measurements. *Journal of Geophysical Research: Oceans* **116** (2011).

[59] Mulet, S. *et al.* The new cnes-cls18 global mean dynamic topography. *Ocean Science* **17**, 789–808 (2021). URL https://os.copernicus.org/articles/17/789/2021/.

[60] Schaeffer, P., Bruinsma, S. & Reinquin, F. The new cnes-cls 2022 marine gravity anomaly model: first validation in the mediterranean. 62 (2022).

[61] Drusch, M. *et al.* Sentinel-2: Esa's optical high-resolution mission for gmes operational services. *Remote sensing of Environment* **120**, 25–36 (2012).

[62] Binet, R., Bergsma, E. & Poulain, V. Accurate sentinel-2 inter-band time delays. *ISPRS Annals of the Photogrammetry, Remote Sensing and Spatial Information Sciences* **1**, 57–66 (2022).

[63] Welsh, P. D. The use of fast Fourier transform for the estimation of power spectra: a method based on time averaging over short, modified periodograms. *IEEE Trans. Audio and Electroacoustics* **15**, 70–73 (1967).

[64] Kramer, M. A. *An Introduction to Field Analysis Techniques: The Power Spectrum and Coherence* (2014). URL https://api.semanticscholar.org/CorpusID:186203068.

[65] Yurovskaya, M. *et al.* Wave spectrum retrieval from airborne sunglitter images. *Remote Sensing of Environment* **217**, 61 – 71 (2018). URL http://www.sciencedirect.com/science/article/pii/S0034425718303596.

[66] Rodriguez, E. & Martin, J. Theory and design of interferometric synthetic aperture radars **139**, 147–159 (1992).

[67] Rodriguez, E. On the optimal design of doppler scatterometers. *Remote Sensing* **10**, 1765 (2018).

[68] Kudryavtsev, V., Yurovskaya, M., Chapron, B., Collard, F. & Donlon, C. Sun glitter imagery of ocean surface waves. part 1: Directional spectrum retrieval and validation. *Journal of Geophysical Research: Oceans* **122**, 1369–1383 (2017).

[69] Kirby, J. T. & Chen, T.-M. Surface waves on vertically sheared flows: approximate dispersion relations. *Journal of Geophysical Research* **94**, 1013–1027 (1989).

[70] Smeltzer, B. K., Æsøy, E., Ådnøy, A. & Ellingsen, S. Å. An improved method for determining near-surface currents from wave dispersion measurements. *Journal of Geophysical Research: Oceans* **124**, 8832–8851 (2019).

[71] Alpers, W. R. Theory of radar imaging of internal waves. *Nature* **314**, 245–247 (1985).

[72] Rascle, N., Chapron, B., Ponte, A., Ardhuin, F. & Klein, P. Surface roughness imaging of currents shows divergence and strain in the wind direction. *Journal*

Of Physical Oceanography **44**, 2153–2163 (2014).

[73] Kudryavtsev, V., Akimov, D., Johannessen, J. & Chapron, B. On radar imaging of current features: 1. Model and comparison with observations. *Journal of Geophysical Research-Oceans* **110**, C07016 (2005).

[74] da Silva, J., Magalhaes, J., Santos-Ferreira, A. M. & Huerre, R. Longevity of internal solitary waves in the pacific cold tongue: Synergies with swot. *Remote Sensing of Environment* **331**, 115038 (2025).

[75] Webb, E. Ratio of spectrum and structure-function constants in the inertial subrange. *Quarterly Journal of the Royal Meteorological Society* **90**, 344–346 (1964).

[76] Babiano, A., Basdevant, C. & Sadourny, R. Structure functions and dispersion laws in two-dimensional turbulence. *Journal of Atmospheric Sciences* **42**, 941–949 (1985).

[77] Sérazin, G. *et al.* Scale-dependent analysis of in situ observations in the mesoscale to submesoscale range around new caledonia. *Ocean Science Discussions* **2019**, 1–32 (2019).

[78] Erickson, Z. K. *et al.* The vertical structure of open-ocean submesoscale variability during a full seasonal cycle. *Journal of Physical Oceanography* **50**, 145–160 (2020).

[79] Callies, J., Barkan, R. & Garabato, A. N. Time scales of submesoscale flow inferred from a mooring array. *Journal of Physical Oceanography* **50**, 1065–1086 (2020).

[80] Balwada, D., LaCasce, J. H. & Speer, K. G. Scale-dependent distribution of kinetic energy from surface drifters in the gulf of mexico. *Geophysical Research Letters* **43**, 10–856 (2016).

[81] Pearson, J. *et al.* Biases in structure functions from observations of submesoscale flows. *Journal of Geophysical Research: Oceans* **125**, e2019JC015769 (2020).

[82] Lindborg, E. A helmholtz decomposition of structure functions and spectra calculated from aircraft data. *Journal of Fluid Mechanics* **762**, R4 (2015).

[83] Wang, H. & Bühler, O. Anisotropic statistics of lagrangian structure functions and helmholtz decomposition. *Journal of Physical Oceanography* **51**, 1375–1393 (2021).

[84] Taylor, S., Thompson, A. F., Kachelein, L. & Klein, P. Seasonal to interannual cross-scale energy transfer variability: Observational insight from the santa barbara channel. *Geophysical Research Letters* **53**, e2025GL117885 (2026).

[85] Rocha, C. B., Chereskin, T. K., Gille, S. T. & Menemenlis, D. Mesoscale to submesoscale wavenumber spectra in drake passage. *Journal of Physical Oceanography* **46**, 601–620 (2016).

[86] Anadon, C. *et al.* Swot-karin level-3 and level-4 algorithms and products overview. Tech. Rep., Copernicus Meetings (2025).

Extended data

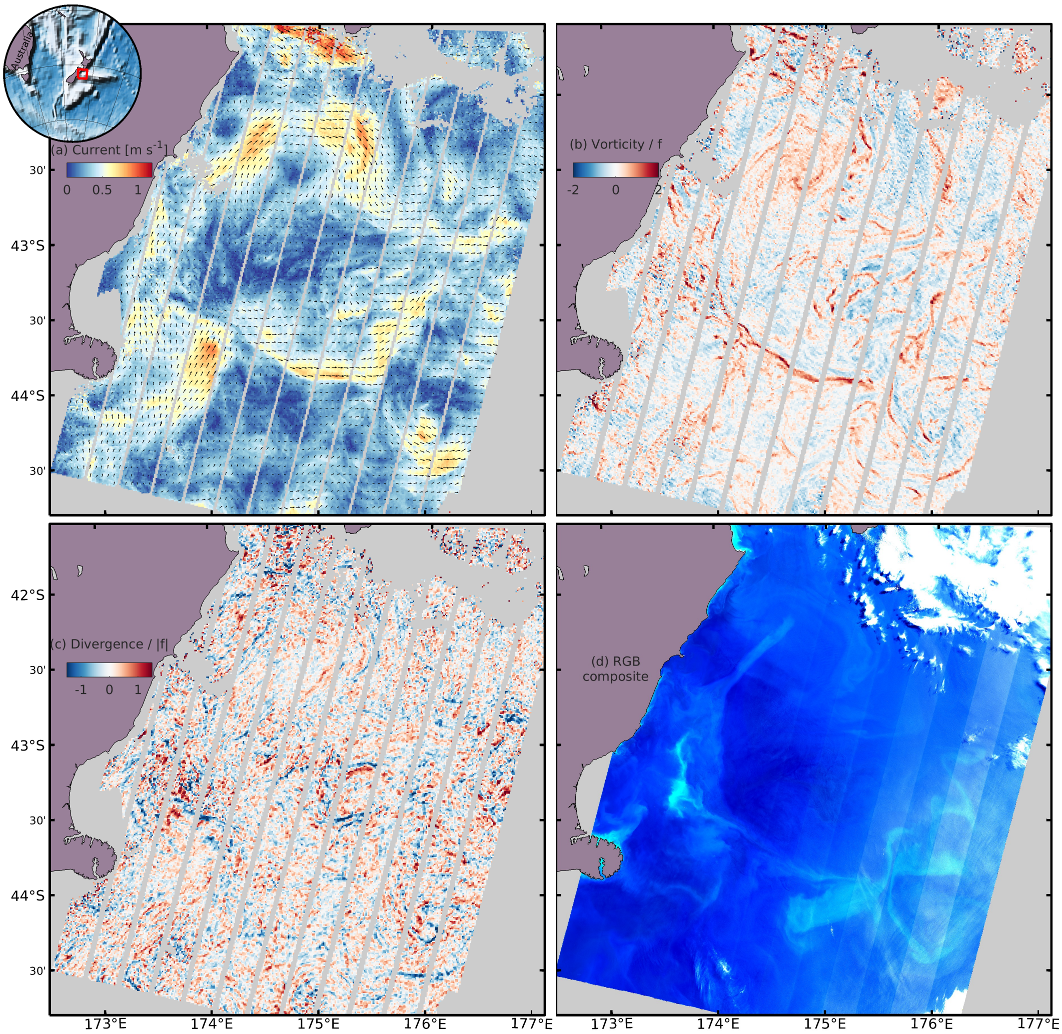

Extended Fig. 1 OT reveals the currents associated with a phytoplankton bloom off New Zealand. (a-c) Currents computed from OT on 10 Dec 2024 at 22:16 UTC. Panel (a) shows the current magnitude with arrows at half resolution. The globe inset shows the location on Earth with the ocean topography. Panels (b) and (c) are the current vorticity and divergence, normalized by the planetary vorticity. The missing data in grey are clouds and coastal water depth less than 30 m. (d) The bloom appears on the original Sentinel-2 color composite image. Note the sharp agreement between observed current fronts and color structures.

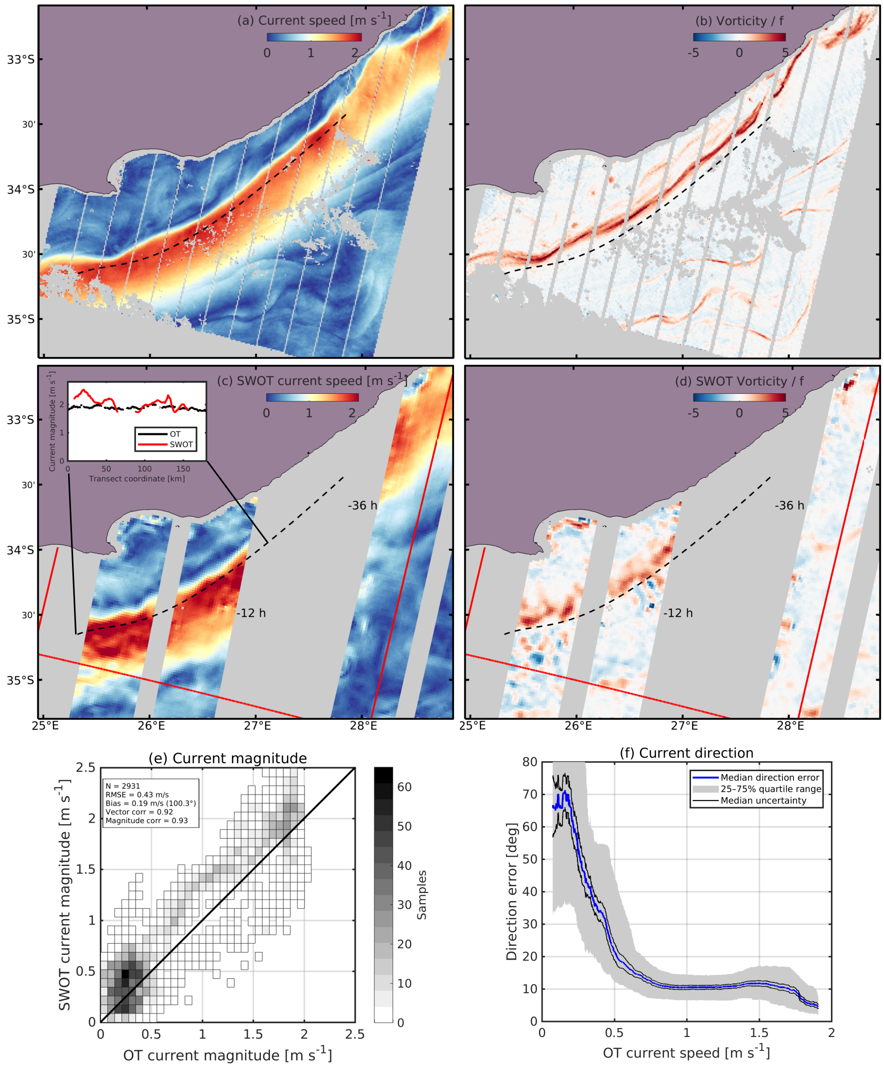

Extended Fig. 2 The Agulhas Current exhibits a filamentary structure with OT while appearing filled with instabilities with swath altimetry. (a,b) Same as Fig. 2, i.e. current and vorticity computed from OT on 11 Dec 2024 at 08:20 UTC. **(c,d)** Composite of two swaths of SWOT geostrophic current (level3 v2.0.1) and vorticity, respectively 12 hours (western tracks) and 36 hours (eastern tracks) before OT, at 20:29 on 9 and 10 Dec 2024. **Inset (c)** highlights the low variability of the Agulhas Current core along the dashed transect. **(e,f)** Magnitude and direction comparisons between OT and SWOT currents display a good overall agreement.

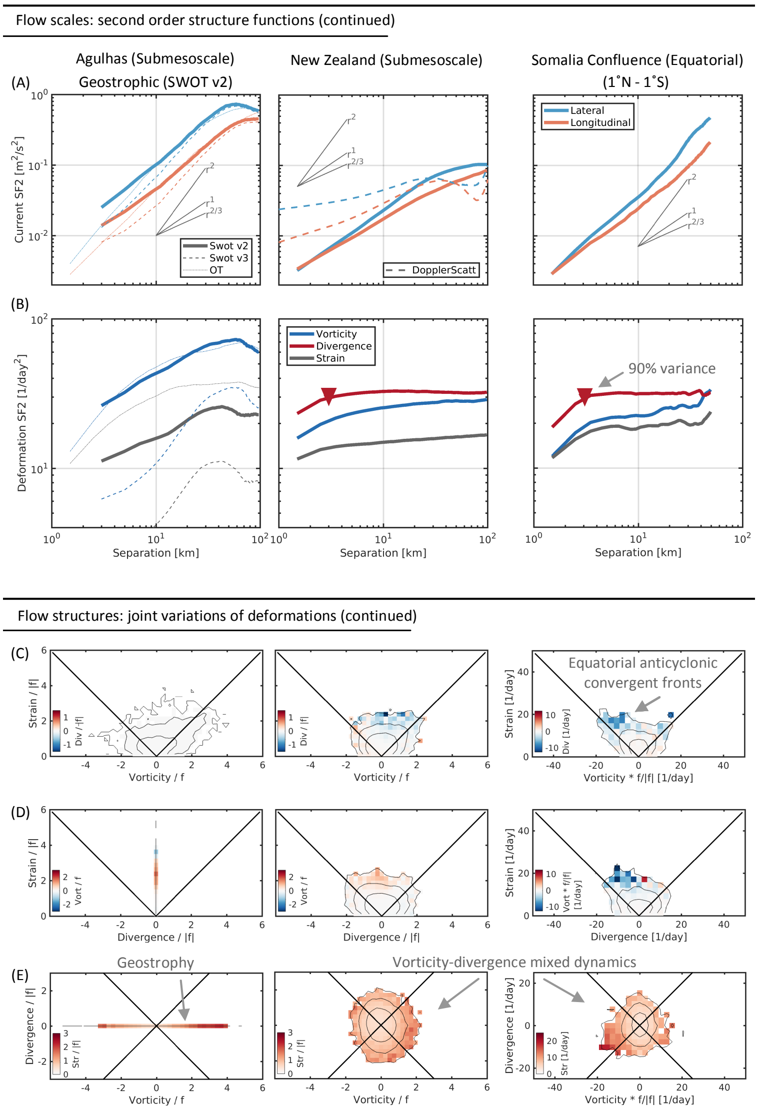

Extended Fig. 3 Beyond geostrophy (continued): OT reveals flow scales and coherent structures across submesoscale, internal-wave and equatorial dynamical regimes. Continued from Fig. 3 with additional dynamical regimes. (Left) In the Agulhas case, SWOT geostrophic currents observed 12 hours before OT show enhanced variability in level 3 v2.0.1 compared with the more filtered level 3 v3 product, although strain variability remains substantially weaker than in OT. (Middle) The New Zealand case provides a mid-latitude example in which vorticity does not dominate divergence. (Right) The Somalia confluence region (1°N-1°S) exhibits the distinctive dynamics of anticyclonic convergent equatorial fronts. For the New Zealand case, airborne DopplerScatt radar observations from California[51] are shown for comparison and exhibit shallower structure-function slopes (Method 4) than the OT observations across all dynamical regimes.

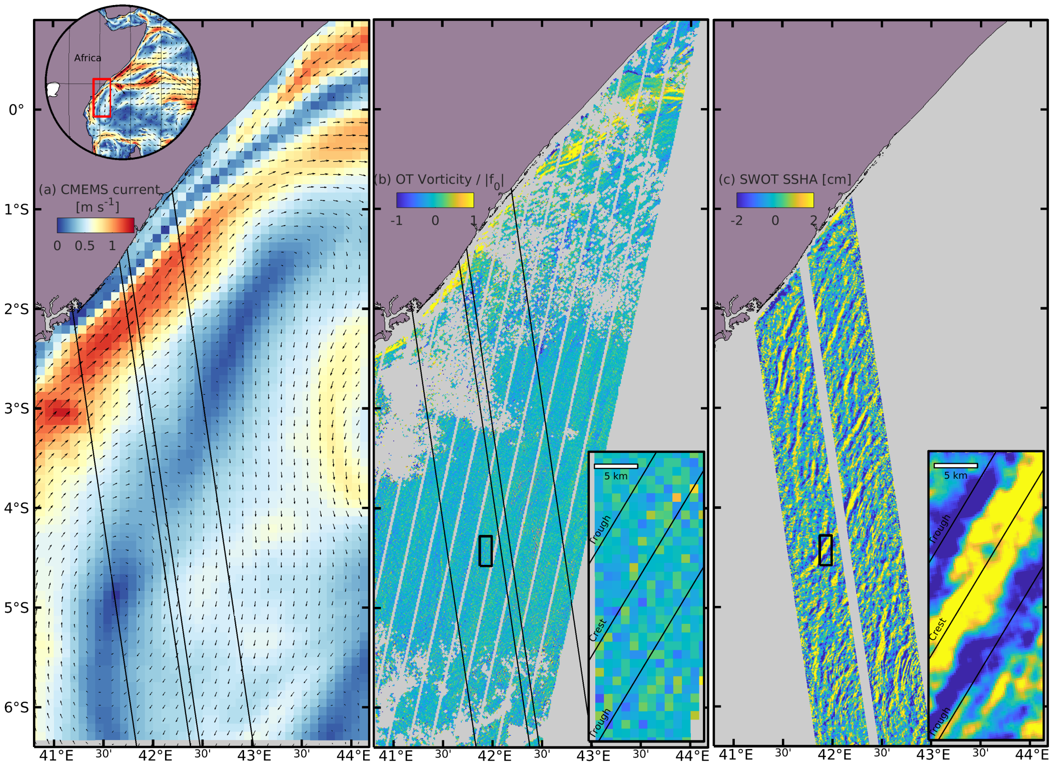

Extended Fig. 4 Additional data for the case of Somalia (Fig. 4). (a) Model analysis from CMEMS (Global Ocean Physics Analysis and Forecast) at the hour of the OT pass, showing the Somali coastal current reversal approximately at the same latitude as observed by OT. The inset shows a larger view of the modelled ocean circulation in the area. **(b)** The vorticity observed by OT is very weak except for intense anticyclonic filaments at the coast and at the equatorial confluence. **(c)** The SSH observed by SWOT closely matches the internal wave patterns seen on OT current divergence and on the SWOT σ_0 field, with 90° phase shift ahead of the internal waves (towards the northwest).

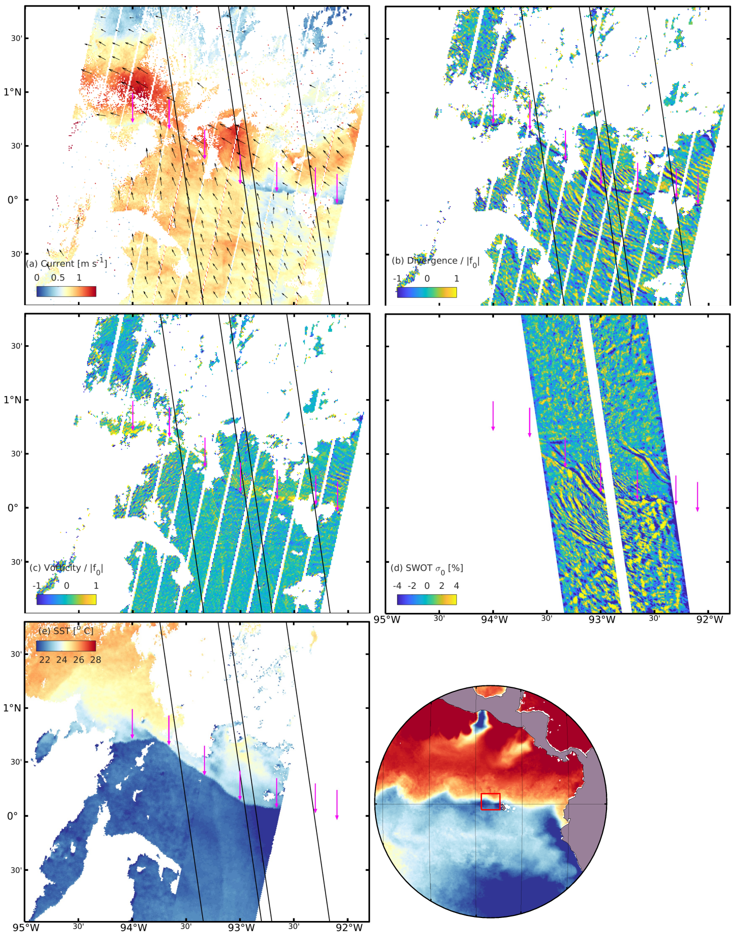

Extended Fig. 5 Equatorial currents of a Pacific tropical instability wave near the Galapagos Islands. (a-c) Currents computed from OT on 14 Dec 2024 at 16:44 UTC. Panel **(a)** shows the current magnitude, with arrows downsampled to a 15 km resolution. Panels **(b)** and **(c)** show the current vorticity and divergence, normalized by $f_0 = 10^{-4}$ s^{-1}. Missing data in white indicate cloud cover. **(d)** Radar cross section σ_0 observed by SWOT 20 minutes earlier (16:24), band-pass filtered over $1-10$ km and expressed as a contrast to background in %. **(e)** Sea surface temperature observed by Sentinel-3 16 minutes earlier (16:28). The globe inset shows a larger view of equatorial Pacific SST observed from microwave radiometers (REMSS). Internal waves are clearly visible in both OT divergence and SWOT σ_0. The equatorial SST front (marked by magenta arrows) exhibits a sharp, kilometre-scale line of convergence, together with weaker vorticity of alternating sign.

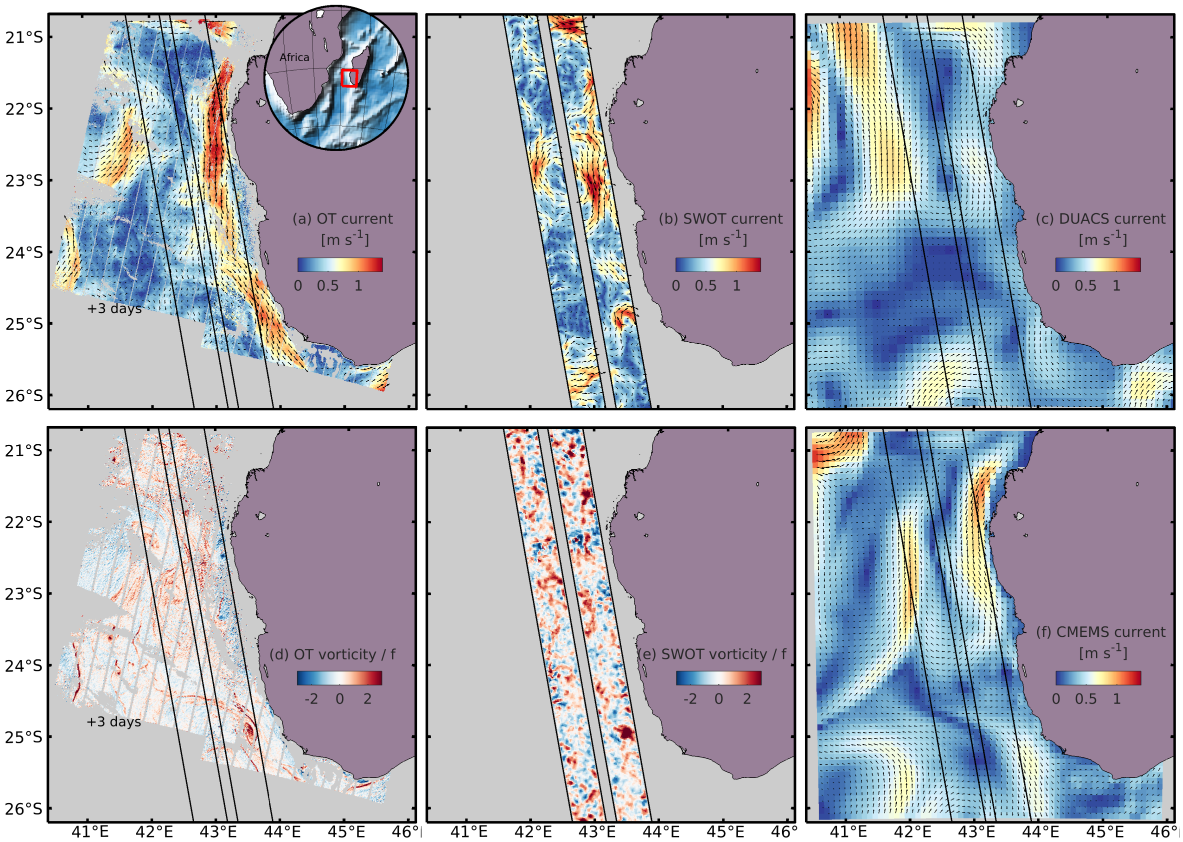

Extended Fig. 6 Altimetry and numerical models underestimate the Southwest Madagascar Coastal Current (SMACC). **(a,d)** OT current and vorticity from a time composite between 13 Dec 2024 at 07:18 UTC (eastern swath) and 16 Dec 2024 at 07:22 UTC (western swath) display a coherent SMACC with mostly filamentary cyclonic vorticity. **(b,e)** Geostrophic current (level3 v3) and vorticity observed by SWOT 38 minutes later on 13 Dec 2024 (07:56 UTC) exhibit more discontinuous SMACC with more turbulent submesoscale eddies. **(c)** Geostrophic current derived from classical altimetry by AVISO-DUACS. **(f)** Numerical analysis from CMEMS. The SMACC appears too weak in models and classical altimetry, and appears discontinuous in swath altimetry.

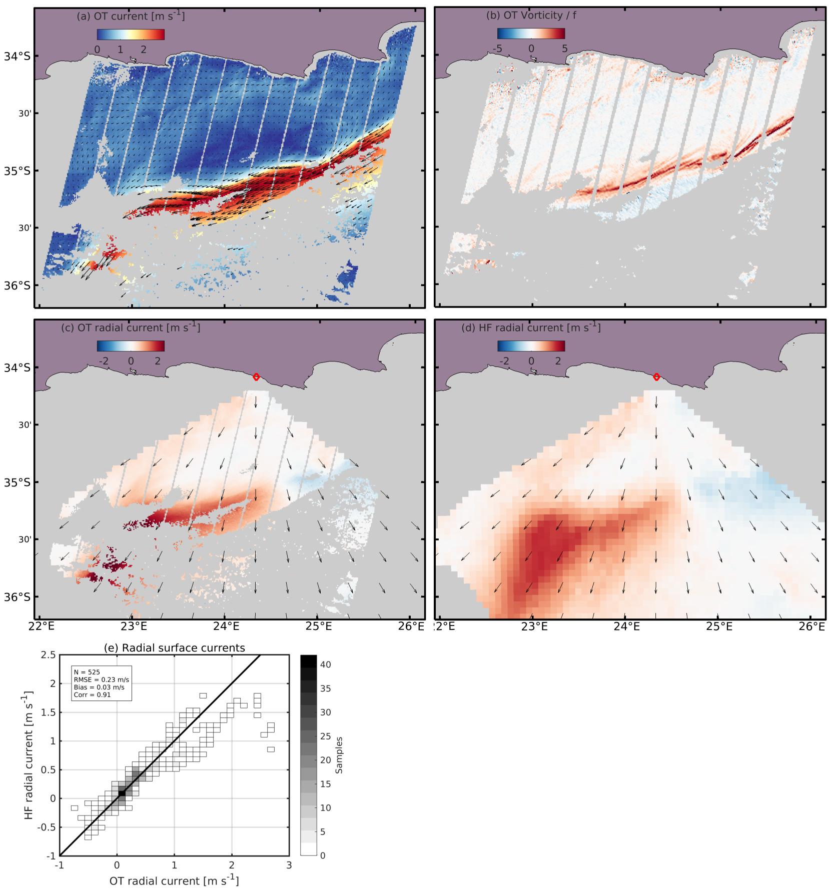

Extended Fig. 7 OT validation over the Agulhas current with HF radar radial velocities. (a,b) OT current and vorticity computed on 22 Feb 2026 at 07:58 UTC. This validation case corresponds to a different location and date than the Agulhas case (11 Dec 2024) discussed throughout the main text. **(c)** OT radial velocity in the direction of the HF radar station (red diamond). **(d)** HF radar radial velocity averaged over 4 hours and every 6 km. **(e)** Radial velocities of OT and the radar display a good overall agreement.

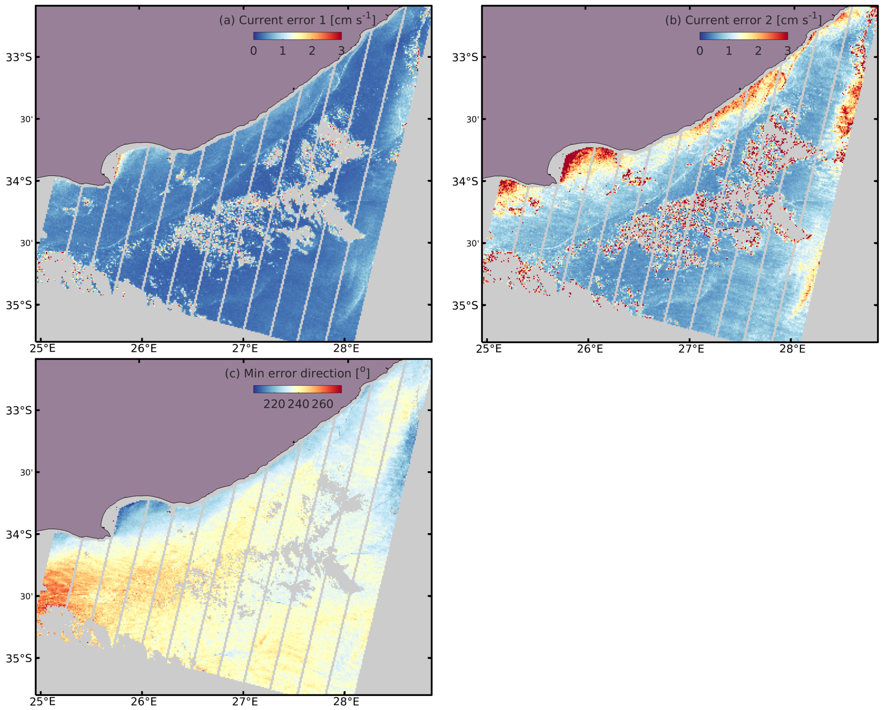

Extended Fig. 8 OT current precision over the Agulhas Current, computed on 11 Dec 2024 from the Hessian of the cost function and the observed phase variance. Shown are the standard errors (1σ) in the best **(a)** and worst **(b)** directions, and **(c)** the azimuth (clockwise from North) of the best-constrained direction.